[American Journal of Science, Vol. 318, April, 2018, P. 367–408, DOI 10.2475/04.2018.01]

American Journal of Science

APRIL 2018

OPEN OCEAN VS. CONTINENTALLY-DERIVED IRON CYCLES ALONG THE NEOARCHEAN CAMPBELLRAND-MALMANI CARBONATE PLATFORM, SOUTH AFRICA

SUEMEYYA EROGLU*,**,†, RONNY SCHOENBERG*, SAKURA PASCARELLI***, NICOLAS J. BEUKES§, ILKA C. KLEINHANNS*, and ELIZABETH D. SWANNER**

ABSTRACT. **The deposition of large amounts of mixed-valence Fe minerals in iron formations during the Archean and Paleoproterozoic indicates that the $Fe(II)_{aq}$ (aqueous) content of coeval anoxic seawater was likely several hundred μM, compared to *ca.* 1 to 20 nM of the modern oxygenated ocean. It has been suggested that oxygen production along shallow marine continental shelves, which probably started several hundred million years before the rise of atmospheric oxygen, effectively oxidized $Fe(II)_{aq}$ from deeper seawater and removed it as $Fe(III)_{ppt}$ (poorly soluble precipitates). However, the reconstruction of the marine Fe cycle during the Archean is still incomplete, partly because of diagenetic redox processes that challenge the interpretation of Fe concentration and isotope signatures of sedimentary archives.**

In this study, we present new Fe concentrations and isotope compositions of carbonate and mudrock samples from the Neoarchean Campbellrand-Malmani carbonate platform (CMCP) in South Africa. These samples are from the shelf facies of the CMCP and in combination with previously published data of Czaja and others (2012) from carbonates and mudrocks of the slope facies, we show that different depositional settings and conditions resulted in different data distributions. Coupled $\delta^{56}Fe$ values (−3.685 to +0.083 ‰) and iron concentrations (861–27672 μg g^{-1}) of pure carbonates deposited during open marine conditions, can be explained by partial Fe(II) oxidation between ferruginous deeper water and oxygenated shallow water, leaving the residual $Fe(II)_{aq}$ pool isotopically light, although Fe(II) oxidation by anoxygenic phototrophy cannot be ruled out. Pure carbonates deposited in a peritidal setting, with less exposure to open ocean water, show a smaller Fe isotope variability with $\delta^{56}Fe$ values of −1.207 to −0.204 permil and Fe concentration range from 388 to 5413 μg g^{-1}, respectively. We propose that the Fe systematics of peritidal carbonates were dominated by early diagenetic Fe cycling between carbonates and adjacent mudrocks.

Synchrotron based X-ray adsorption spectroscopy reveals a change in Fe speciation, where Fe(II)-bearing ankerite and Fe-sulfide dominate the carbonates in the lower part of the CMCP, whereas carbonates of the upper part of the CMCP mainly contain Fe(III)-(oxyhydr)oxides. The fact that Fe(III) phases are still preserved argues for a higher oxidation state on the shelf of the upper CMCP. This is likely because of a lower content of reductants in those settings, in particular organic carbon, sulfide species, as well as restricted influx of reducing species from the anoxic open ocean due to the formation of a rimmed margin. Nevertheless, more studies of similar carbonate settings are necessary to verify our model.

* Department of Geosciences, University of Tuebingen, Wilhelmstraße 56, 72074 Tuebingen, Germany
** Department of Geological and Atmospheric Sciences, Iowa State University, 2237 Osborn Drive, Ames, Iowa 50011-1027, United States of America
*** European Synchrotron Radiation Facility, 38043 Grenoble, France
§ DST-NMF CIMERA, Department of Geology, University of Johannesburg, Auckland Park Kingsway Campus, 2006, South Africa
† Corresponding author: seroglu@geomar.de; present address: GEOMAR Helmholtz Centre for Ocean Research, Wischhofstraße 1-3, 24148 Kiel, Germany

We propose that unfractionated $Fe(II)_{aq}$ in seawater was about two to three times lower on the shelf (30–310 μM) than along the slope (61–928 μM), which implies that $Fe(II)_{aq}$ was removed from the water column closer to the continent, likely by oxidation and precipitation. Overall, the Fe isotope composition and Fe speciation of CMCP sediments support the presence of molecular oxygen in the shallow-marine system and emphasize the utility of Ca-Mg carbonates as proxies for iron cycling in the aqueous environment.

Keywords: Neoarchean ocean, carbonate platform, Redoxcline, Fe isotopes, X-Ray absorption spectroscopy

INTRODUCTION

The concentration of iron (Fe) in seawater over Earth's history largely depends on the ocean's redox state and major changes are linked to the emergence of oxygenic photosynthesis and the Great Oxidation Event (GOE) about 2.46 to 2.33 billion years (Ga) ago (Luo and others, 2016; Gumsley and others, 2017). The occurrence of mixed-valence Fe minerals in iron formations (IF) (fig. 1A) during the Precambrian indicates that seawater had significantly higher concentrations of soluble $Fe(II)_{aq}$ compared to the modern ocean and that $Fe(II)_{aq}$ was removed from seawater by oxidation to form $Fe(III)_{ppt}$ via photosynthetically produced oxygen (Cloud, 1968; Isley and Abbott, 1999). Alternatively, Fe(II) oxidation by anoxygenic photoautotrophic bacteria has been postulated as a way of generating Fe(III)-minerals for IF in the absence of oxygen (Garrels and Perry, 1974; Konhauser and others, 2002; Kappler and others, 2005; Crowe and others, 2008). In the modern oxygenated ocean, $Fe(II)_{aq}$ concentrations are normally between 1 and 20 nM (for example Landing and Bruland, 1987; Martin and others, 1990; de Baar and de Jong, 2001), which is much lower than estimates for the Archean anoxic ocean, ranging from 3 to 360 μM (Holland, 1973; Morris, 1993; Canfield, 2005). Some of these estimates are based on the solubility product of siderite and calcite under the assumption of oversaturation and direct precipitation of those two minerals from seawater (Holland, 1973; Holland, 2004; Canfield, 2005). However, recent studies indicate that some siderite does not form by direct precipitation from seawater but rather as a diagenetic product (Johnson and others, 2003; Johnson and others, 2008b; Fischer and others, 2009; Heimann and others, 2010; Johnson and others, 2013), undermining siderite saturation in seawater as a valid assumption for Fe concentration estimates. Other calculations are based on estimates of hydrothermal activity during Archean times and silica concentrations of coeval seawater (Morris, 1993). Recent work considering greenalite formation suggests 0.9 to 12 μM $Fe(II)_{aq}$ in the deep ocean (Tosca and others, 2016). Herzog and others (1989) showed that at $Fe(II)_{aq}$ concentrations higher than 10 μM, calcite precipitation would be inhibited. Riding and others (2014) thus proposed that $Fe(II)_{aq}$ concentrations in the Archean shallow-marine environment must have been below 10 μM in order to allow the apparent calcite precipitation.

The massive deposition of IF along continental shelves began several hundred million years (between 2.8 and 2.4 Ga) before the GOE. This overlaps within the suggested time range for the onset of oxygen production by oxygenic photosynthesis, represented by the chemical equation:

$$H_2O + CO_2 + h\nu \rightarrow CH_2O + O_2 \qquad (1.1)$$

in the shallow marine environment (for example Anbar and others, 2007; Wille and others, 2007; Frei and others, 2009; Voegelin and others, 2010; Voegelin and others, 2010; Crowe and others, 2013; Eroglu and others, 2015; Kurzweil and others, 2015b). The Fe-(oxyhydr)oxides, -sulfides, and -carbonates, bulk IF, bulk mudrocks, and Ca-Mg carbonates deposited during this time show highly variable $\delta^{56}Fe$ signatures, with

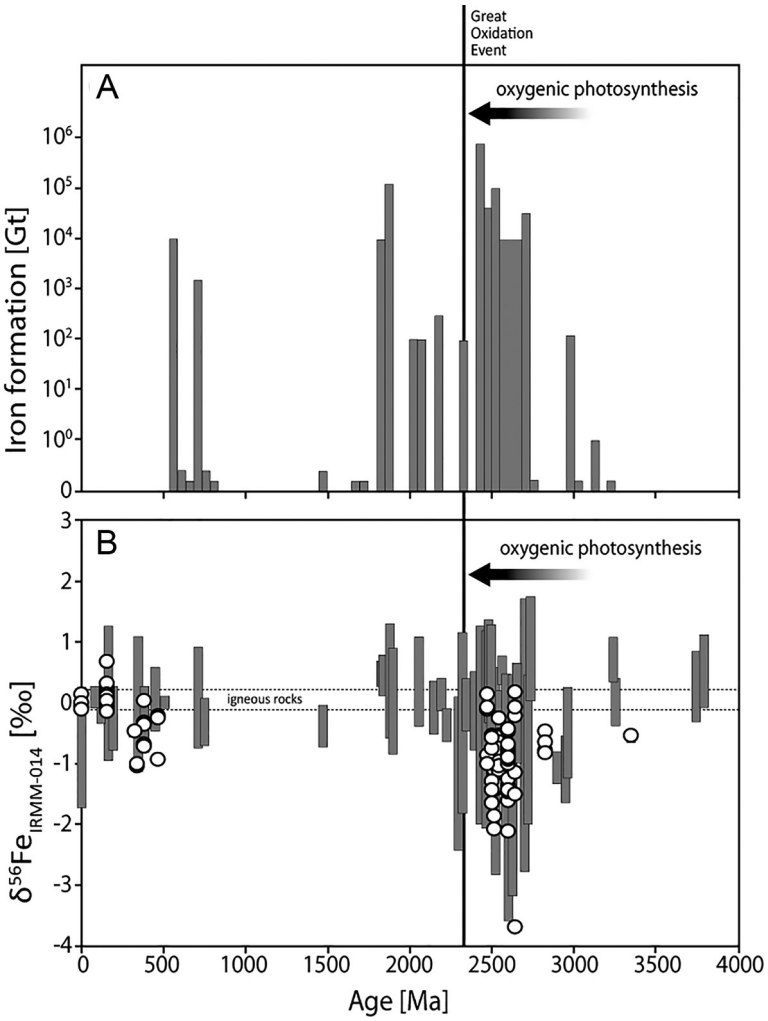

Fig. 1. (A) Appearance of Banded Iron Formations over Earth's history [modified from Bekker and others (2010)]. (B) Compilation of δ^{56}Fe isotope signatures, analyzed on bulk IF, hydrothermal deposits, bulk mudrocks, Fe(oxyhydr)oxides, carbonates, and –sulfides [modified from Busigny and others (2014)]. White circles are data from Ca-Mg carbonates (Matthews and others, 2004; Heimann and others, 2010; von Blanckenburg and others, 2008; Craddock and Dauphas, 2011; Czaja and others, 2012).

excursions down to −3.68 permil (fig. 1B) (Johnson and others, 2003; Rouxel and others, 2005; Yamaguchi and others, 2005; Johnson and others, 2008c; Heimann and others, 2010; Steinhoefel and others, 2010; Planavsky and others, 2012; Czaja and others, 2012). Partial oxidation of anoxic and iron-rich (ferruginous) deep seawater along a chemical gradient (chemocline) by oxygen in surface waters according to:

$$4Fe^{2+}_{aq} + O_2 + 8OH^- + 2H_2O \rightarrow 4Fe(OH)_3 \qquad (1.2)$$

leads to the precipitation of isotopically heavy $Fe(III)_{ppt}$, leaving the remaining dissolved $Fe(II)_{aq}$ pool isotopically lighter (Rouxel and others, 2005). Residual isotopically light $Fe(II)_{aq}$ could be recorded in Fe(II)-sulfide and -carbonate minerals, as well as Ca-Mg carbonates.

Fractionation of Fe by anoxygenic photosynthetic Fe(II) oxidation:

$$4Fe^{2+}_{aq} + HCO_3^- + 10H_2O + h\nu \rightarrow 4Fe(OH)_3 + CH_2O + 7H^+ \qquad (1.3)$$

(Hegler and others, 2008), results in a $\varepsilon^{56}Fe_{Fe(III)ppt\text{-}Fe(II)aq}$ of +1 to +3 permil and is thus indistinguishable from biotic or abiotic aerobic oxidation at neutral pH (Bullen and others, 2001; Beard and others, 2003a; Croal and others, 2004; Balci and others, 2006; Kappler and others, 2010; Swanner and others, 2015b). However, the conservation of such an isotopically light Fe seawater reservoir within sediments can be superimposed by benthic microbial dissimilatory Fe(III) reduction (DIR). This process can produce very negative $\delta^{56}Fe$ by partial reduction of Fe oxides and oxidation of organic carbon, reacting to Fe-carbonate, typically siderite (Johnson and others, 2008a; Johnson and others, 2008b; Johnson and others, 2008c; Heimann and others, 2010), as in:

$$4Fe(OH)_3 + CH_2O + HCO_3^- \rightarrow 4FeCO_3 + 3OH^- + 7H_2O \qquad (1.4)$$

The ability of siderite to record primary seawater Fe isotope signatures has been questioned based on the prevalence of secondary diagenetic Fe redox cycling in organic-rich sediments, for example DIR and the precipitation and dissolution processes of Fe(II) sulfide (Matthews and others, 2004; Yamaguchi and others, 2005; Rouxel and others, 2006; Yamaguchi and Ohmoto, 2006; Johnson and others, 2013).

Microbial Ca-Mg carbonates are valuable archives of ancient seawater chemistry, as the carbonate precipitation from seawater causes minor to no elemental fractionation of a wide range of trace elements, although precipitation rate, temperature, and concentrations of ions in the seawater influence their distribution coefficient (for example Webb and Kamber, 2000; Sumner and Grotzinger, 2004; Sumner and Beukes, 2006). Therefore, Ca-Mg carbonates have the potential to record geochemical seawater signatures and could be potential proxies for seawater Fe (von Blanckenburg and others, 2008; Johnson and others, 2013). Studies on this subject are scarce (Matthews and others, 2004; Dideriksen and others, 2006; von Blanckenburg and others, 2008; Heimann and others, 2010; Craddock and Dauphas, 2011; Czaja and others, 2012), but provide some interesting observations. The most important is that $Fe(II)_{aq}$ from fluids is incorporated into Ca-Mg carbonates without any isotope fractionation (Dideriksen and others, 2006; von Blanckenburg and others, 2008). Furthermore, some studies indicate that dolomitization does not affect the original Fe isotope signature of carbonates, as there is no difference in the isotope signature between limestones and dolomites, or a dependence on the Mg content (von Blanckenburg and others, 2008; Heimann and others, 2010; Czaja and others, 2012; Johnson and others, 2013). However, diagenetic (fluid) alteration, secondary formation of Fe-minerals during early diagenesis, and dissolution of detrital components can influence the Fe inventory of Ca-Mg carbonates and thus challenge the interpretation of seawater Fe geochemistry (Brand and Veizer, 1980; Veizer, 1983; Banner, 1995; Matthews and others, 2004; Heimann and others, 2010; Craddock and Dauphas, 2011; Czaja and others, 2012; Hodgskiss and others, 2018). Matthews and others (2004), for instance, clearly showed that Ca-Mg carbonates are locally affected by adjacent mudrocks in the course of diagenetic Fe circulation in the sediment and proposed a diffusional Fe isotope exchange between the carbonate and porewater. Nevertheless, it is important to point out that Ca-Mg carbonates are strongly influenced by the ambient fluid, such as bottom-water or porewater. Seawater and/or freshwater will mainly influence the Fe content and isotope signature of the bottom- and porewaters of these carbonates, unless if Fe from siliciclastic material or Fe-oxides is remobilized in the sediment. Thus, Ca-Mg carbonates are good candidates to reflect the Fe isotope signatures of seawater, freshwater, and porewater, as well as indicate the processes that resulted in these

signatures. In order to distinguish these signals and correctly interpret these Fe signatures a comprehensive understanding of the depositional environment from major and trace element signatures and sedimentological observations is necessary.

Here, carbonate and mudrock samples of the 2.58 to 2.50 Ga old Campbellrand-Malmani carbonate platform (CMCP) succession in southern Africa were analyzed for their Fe isotope composition and concentration. Several studies have shown that the CMCP is well preserved and partly reflects valuable seawater signatures (for example Beukes, 1987; Sumner and Grotzinger, 2004; Eroglu and others, 2015; Eroglu and others, 2017). These results were combined with X-ray absorption spectroscopy (XAS) data of representative rock sections to examine the Fe-redox speciation and mineralogy. The Fe isotope data of shelf facies from this study are combined with published Fe isotope data of the slope facies (Czaja and others, 2012) and with elemental data from Eroglu and others (2015). The goal is to reconstruct the Fe cycling in a shallow-marine, possibly oxygen-producing, carbonate platform system and to decipher the factors controlling the Fe inventory.

GEOLOGICAL OVERVIEW

The CMCP is the lower sedimentary succession of the Transvaal Supergroup (TSG) in southern Africa (fig. 2A) and was deposited between ~2.58 and 2.50 Ga (Sumner and Beukes, 2006). It is preserved in the Transvaal area (TA) in the eastern part, the Griqualand West area (GWA) and Prieska area in the western part of the Kaapvaal Craton, as well as the Kanye area in the north-central part of the platform (fig. 2A).

Except for some carbonate segments in the eastern TA that were affected by contact metamorphism related to the intrusion of the Bushveld Complex (Frauenstein and others, 2009), the majority of the CMCP experienced conditions no higher than lower greenschist facies metamorphism (Button, 1973; Miyano and Beukes, 1984), covering temperatures between about 250 to 330 °C (Eroglu and others, 2017). The TA contains the Malmani Subgroup, which is represented in the KMF-5 drill core that preserves four (out of five) formations showing dominantly peritidal (inter- to supratidal) and partly silicified dolomite, subordinate shallow subtidal dolomite, and occasional interbeds of fine siliciclastic mudrocks from marine regression events (Eroglu and others, 2015). The sediments of the contemporaneous Campbellrand Subgroup in the GWA are represented in seven formations in the BH-1 drill core that can be stratigraphically correlated with the Malmani Subgroup and mainly reflect shallow subtidal conditions (fig. 2B). Further to the southwest in the marginal and basinal sequence (Prieska area) the sedimentation rates decreased, which resulted in a diminished thickness (~500 m) in the slope area compared to the *ca.* 2000 m thick shelf succession (fig. 2B). Altermann and Nelson (1998) estimated sedimentation rates of 2 to 20 m/Ma for the slope succession and 50 to 150 m/Ma for the shelf succession.

The depositional conditions of the CMCP have been reconstructed in geochemical and sedimentological studies of four drill cores, the GKP01 and GKF01 drill cores from the Prieska facies, the BH-1 drill core from the GWA, and the KMF 5 drill core from the TA (Beukes, 1987; Schröder and others, 2006; Sumner and Beukes, 2006; Knoll and Beukes, 2009; Eroglu and others, 2015). Here, the focus is on the shelf facies, represented in the sediments of the KMF-5 and the BH-1 drill cores, as well as the Kuruman Kop outcrop, which contains carbonates from the shelf facies of the upper Campbellrand Subgroup (Sumner, 2002). Well preserved carbonate intervals were sampled for this study, with good preservation of sedimentary textures and structures. Veined, crackle brecciated and coarsely recrystallized intervals were avoided. Additionally, samples of silicified dolomite and siliciclastic mudrocks were taken. Detailed descriptions of KMF-5 and BH-1 are provided by Eroglu and others (2015) and Altermann and Siegfried (1997), respectively.

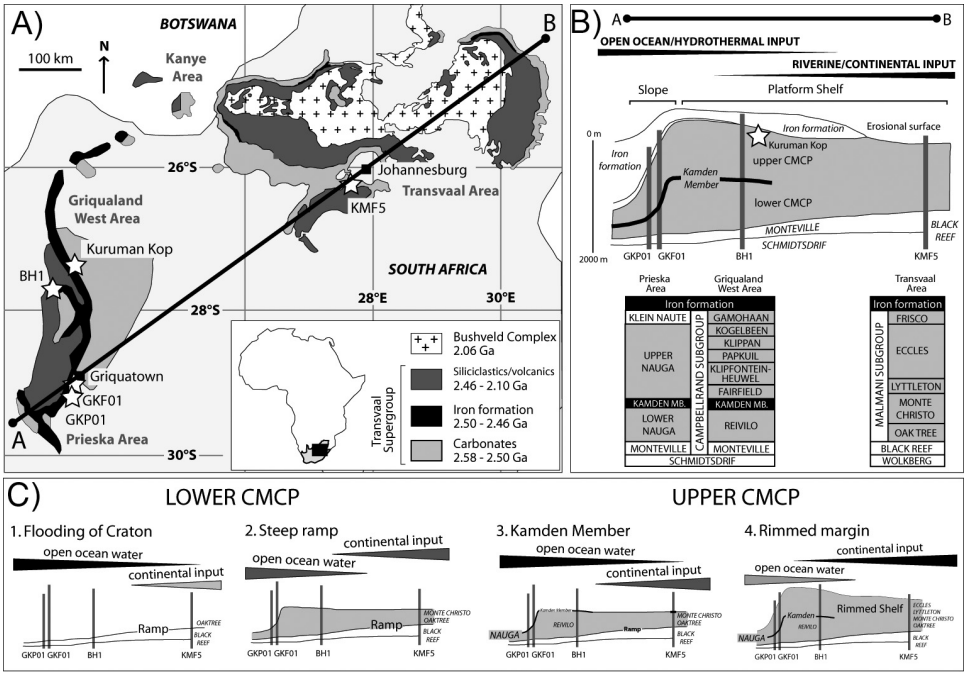

Fig. 2. (A) Geological overview of the Transvaal Supergroup (TSG). Asterisks indicate locations of drill cores from the slope facies (GKP01, GKF01) and the shelf facies (BH-1, KMF-5). Modified after Coetzee (ms, 2001) and Sumner and Grotzinger (2004). (B) A-B cross section through chemical sediments of the lower TSG and a schematic location of drill cores GKP01, GKF01, BH-1, and KMF-5. Asterisk represents the Kuruman Kop. Depositional conditions of CMCP were controlled by influx of open ocean water and freshwater from the continent. The CMCP can be divided into slope facies and shelf facies. The platform is preserved in several formations, indicated in gray (Kamden Mb. = Kamden Member). Modified after Beukes and Gutzmer (2008) and Eroglu and others (2015). (C) Paleoenvironmental reconstruction of the CMCP over time with relative influxes of open ocean and freshwater (modified after Eroglu and others, 2017). The CMCP can be subdivided into the lower and the upper CMCP, deposited during four stages. 1) Flooding of the Kaapvaal Craton: high influx of hydrothermal water from the open ocean decreases with the build-up of the platform. 2) Influence of continental material increases: frequent deposition of mudrocks in peritidal environment (Monte Christo formation). 3) Short intense transgression and deposition of Kamden Member: increased influx of hydrothermally-influenced seawater. 4) Formation of rimmed margin: limited influx of open ocean water and higher influence of continental fluids.

Sedimentology of the succession reveals that the CMCP experienced several trans- and regression events during changing influx of water masses from the open ocean and from the continent. Even though most of the CMCP is dolomitized, sedimentological features and structures (Beukes, 1987; Sumner and Beukes, 2006) as well as some primary geochemical signals (Eroglu and others, 2015; Eroglu and others, 2017) are still preserved. Importantly, Fe and Mn concentrations and REE+Y signatures correlate with the stratigraphy, water depth, and the input of hydrothermal or continental fluids (Voegelin and others, 2010; Eroglu and others, 2015; Eroglu and others, 2017). This allows reconstruction of the environmental conditions and the evolution of this carbonate platform (Eroglu and others, 2015; Eroglu and others, 2017), which can be divided into a *lower* and an *upper CMCP* (fig. 2C). The *lower CMCP* reflects a steep ramp architecture and includes the stratigraphical correlative formations Lower Nauga from the Campbellrand Subgroup (GKP01, GKF01; Prieska area), Reivilo from the Campbellrand Subgroup (BH-1; GWA), and Oaktree and Monte Christo from the Malmani Subgroup (KMF-5; TA) (fig. 2B). During the initial flooding of the Kaapvaal Craton

and incipient carbonate deposition, the samples of the lower Oaktree Formation show elevated Fe/Mn and HREE/LREE signatures (Eroglu and others, 2017) that are characteristic for hydrothermal fluids from mid-ocean ridges (Pearce, 1983). Fe and Mn concentrations in carbonates decrease and Y/Ho ratios increase in the upper Oaktree Formation with the build-up of the platform, indicating a decreasing influx of hydrothermally influenced water (fig. 2C – stage 1) (Eroglu and others, 2017). After the build-up of the steep ramp platform and during a regression, the peritidal Monte Christo Formation and the lagoonal Reivilo Formation were deposited. During this stage more continental material was deposited and is preserved in the Monte Christo Formation as organic-rich mudrocks. Fe/Mn ratios are more variable and REE+Y signatures imply a continental source in this part of the section, indicating redistribution of Fe between mudrock and carbonate layers and a stronger influence of continental meteoric water (fig. 2C – stage 2) (Eroglu and others, 2015; Eroglu and others, 2017). The Kamden 'Iron Formation' Member was deposited on top of the lower CMCP during a temporary major transgression and is geochemically visible in Fe-rich rocks throughout the CMCP (Sumner and Beukes, 2006). The TA does not contain the Kamden Member, however, the stratigraphically correlative, siliciclastic carbonate sample 1265.2 in KMF-5 has a high Fe_2O_3 content (>10 wt-%), which indicates increased influence of hydrothermal fluids from the open ocean water, probably during a short intense transgression and the deposition of the Kamden Member (fig. 2C – stage 3) (Eroglu and others, 2015). The *upper CMCP* reflects a rimmed margin architecture and includes the formations Upper Nauga from the Campbellrand Subgroup (GKP01, GKF01; Prieska area), Fairfield, Klipfonteinheuwel, Papkuil, Klippan, Kogelbeen, and Gamohaan from the Campbellrand Subgroup (BH-1, Kuruman Kop; GWA), and Lyttleton and Eccles from the Malmani Subgroup (KMF-5; TA). Due to the rimmed margin the influx of open ocean water was likely restricted and instead the influence from continental fluids increased, which is implied by variable Fe/Mn ratios and 'continental' REE+Y signatures (fig. 2C – stage 4) (Eroglu and others, 2017). In this context it should be noted that the draw-down of hydrothermal influx onto the shallow-water shelf might have induced an evolutionary advantage for oxygenic photosynthesis, which does not rely on reduced species such as are needed for anoxygenic photosynthesis, and therefore set the stage for the development of a thriving aerobic ecosystem (for example Des Marais, 2001).

METHODS

Fe Isotope Analyses

Between 15 and 170 mg powdered samples, corresponding to approximately 200 μg of total sample Fe, were weighted into 15 ml perfluoroalkoxy alkanes (PFA) beakers. Sample digestion for carbonates was done using 20 percent acetic acid to avoid digestion of Fe oxides and clay minerals, according to the chemical protocol of von Blanckenburg and others (2008). Mudrocks were completely digested in a 2:1 mixture of distilled HF and HNO_3. Fe purification was achieved using the method described in Schoenberg and von Blanckenburg (2005). Fe isotope measurements were performed on a ThermoFisher Scientific Neptune Plus multicollector-inductively coupled plasma-mass spectrometer (MC-ICP-MS) at the facilities of the Isotope Geochemistry Group, University of Tuebingen, using the standard-sample-bracketing method (Schoenberg and von Blanckenburg, 2005). Fe isotope data are reported relative to the IRMM-014 standard [Institute of Reference Material and Measurements, Geel, Belgium; Taylor and others (1992)] as

$$\delta^{56}\mathrm{Fe}(‰) = \left(\frac{\frac{56\mathrm{Fe}}{54\mathrm{Fe}}^{\mathrm{sample}}}{\frac{56\mathrm{Fe}}{54\mathrm{Fe}}^{\mathrm{IRM014}}} - 1 \right) \times 1000 \quad (3.1)$$

Procedural blanks were between 4 and 13 ng, which is less than 0.1 percent of the total amount of Fe that passed through the Fe purification procedure, and is negligible for the samples' Fe isotope compositions. Repeated measurements of aliquots of the HanFe standard run during analytical sessions gave an average δ^{56}Fe of +0.291 ± 0.060 ‰ (2SD, n = 76), which is in agreement with values published by Kurzweil and others (2015a) (+0.29 ± 0.05 ‰; n = 145). The IF-G reference material gave an average value of +0.643 ± 0.062 ‰ (2SD, n = 13) and is in agreement with values published by Dauphas and Rouxel (2006) (+0.631 ± 0.019, n = 18) and Kurzweil and others (2016) (+0.63 ± 0.02). All samples were measured at least twice and show a good internal reproducibility (tables SM-1, SM-2, SM-3; supplementary material, http://earth.geology.yale.edu/%7eajs/SupplementaryData/2018/Eroglu).

Synchrotron-based X-ray Absorption Spectroscopy

We conducted micro X-ray Absorption Near Edge Structure (μ-XANES) spectroscopy mapping in fluorescence mode (Pascarelli and others, 1999) and transmission mode using the "Turbo-XAS" design at the energy-dispersive X-ray absorption spectroscopy (XAS) beamline ID24 at the European Synchrotron Radiation Facility (ESRF; Pascarelli and others, 2016). The advantage of this beamline is its high acquisition speed, which enables the collection of XANES spectra on every pixel of a map. A Si(111) bent polychromator in the Bragg geometry is used to create a polychromatic fan of radiation focused on the sample position. Vertical focusing is obtained by a bent Si mirror at a grazing incidence angle of 4 mrad. A focal spot size of 5 × 5 μm^2 FWMH was used in this experiment. Harmonic rejection is further achieved with two Si mirrors at 3 mrad grazing incidence angle. In transmission mode, parallel detection of all energy points in the energy range 6.9 to 7.4 keV leads to acquisition times of the order of 20 ms per spectrum. In fluorescence mode, a monochromatic beam is created by placing a fast-moving slit on the polychromatic fan of radiation, and acquisition time for the energy range 7.0 to 7.3 keV is of the order of 11 s per spectrum. Transmission mode maps were collected on an area of 2000 × 2000 μm (20 × 20 μm pixel size) in about the same amount of time as was required to collect 500 × 500 μm maps (between 10 × 10 μm and 50 × 50 μm pixel size) in fluorescence mode. For experiments in fluorescence mode, 30 μm thick polished thin sections mounted on glass slides were prepared. For experiments in transmission mode 100 μm thick unmounted thin sections were prepared.

Fluorescence and transmission data were processed using the PyMCA software package, which allows evaluation of large data sets (Sole and others, 2007). The transmission spectra were calculated as follows:

$$I_1 = I_0 e^{-\mu(E)} \rightarrow \mu(E) * \mathrm{x} = -\ln\frac{I_1}{I_0} \quad (4.1)$$

where μ is the absorption is a function of the energy E, I_0 is the incident X-ray beam intensity, I_1 is the beam intensity after transmission through the sample and x is the sample thickness. For fluorescence spectra, the absorption is defined as $\mu(E) \propto \frac{I_f}{I_0}$, where I_f is the fluorescence intensity. First, all spectra of a selected sample were energy calibrated by analyzing metallic Fe with the same experimental setup as used for

samples (that is, fluorescence or transmission mode) and setting the first inflection of the Fe K-edge to 7112 eV. Subsequently, all spectra were normalized and over- or undersaturated spectra were automatically excluded from further analysis. By selecting specific regions of the XANES spectra (energy range from 7100 to 7175 eV), maps of Fe concentration and oxidation state were generated (figs. S1 a-d; supplementary material, http://earth.geology.yale.edu/%7eajs/SupplementaryData/2018/Eroglu). The edge-jump maps show the intensity of absorption or fluorescence at the Fe edge-jump, which is the qualitative representation of the Fe concentration (Munoz and others, 2006). The oxidation state of Fe is indicated by the main edge position, which is the maximum of the first derivative of the spectra, and is specific to each Fe redox species (O'Day and others, 2004).

RESULTS

Fe Concentration and Isotopic Composition

The Fe concentration and δ^{56}Fe data of carbonates and (siliciclastic) mudrocks from KMF-5, BH-1, and Kuruman Kop are displayed in figure 3 and figures 4A–4D. Carbonates are divided into pure (<1 wt-% Al_2O_3), detritus-containing (>1 wt-% Al_2O_3), and silicified (>3.26 wt-% SiO_2), as in Eroglu and others (2015). Data are complemented with previously published data of carbonates and mudrocks from the slope drill cores GKP01 and GKF01 (Czaja and others, 2012). Analogous to this study, the $\delta^{56}Fe_{carb}$ data (carbonate fraction) of the carbonate samples and the $\delta^{56}Fe_{WR}$ data (whole rock) of the mudrock samples were used (Czaja and others, 2012).

Carbonate and mudrock samples of KMF-5 are listed in table 1. Pure carbonates contain between 1422 and 12941 $\mu g\ g^{-1}$ Fe and have δ^{56}Fe signatures between −0.877 and +0.083 permil. Silicified carbonates show concentrations from 580 to 6270 $\mu g\ g^{-1}$ and δ^{56}Fe signatures from −0.883 to −0.235 permil. Mudrocks show Fe contents between 366 and 1368 $\mu g\ g^{-1}$, which is in the concentration range of the carbonates, although one mudrock shows a very high Fe concentration of 65032 $\mu g\ g^{-1}$. However, δ^{56}Fe signatures of most mudrocks show heavier values between −0.366 and +0.788 permil. The carbonate fraction of Fe- and silicate-rich sample 1265.1 also shows a higher Fe concentration of 17148 $\mu g\ g^{-1}$ and a δ^{56}Fe signature of −0.036 permil.

Carbonate samples of BH-1 are listed in table 2. Pure carbonates show Fe contents between 388 and 9546 $\mu g\ g^{-1}$ and δ^{56}Fe signatures between −1.235 and −0.225 permil. Pure carbonate 375 contains 8526 $\mu g\ g^{-1}$ Fe, and shows a δ^{56}Fe composition of −0.854 permil. The carbonate 1914 has a very high Fe concentration of 27655 $\mu g\ g^{-1}$ and a δ^{56}Fe composition of −0.951 permil. BH-1 samples are dolomites like the KMF-5 samples (~30 wt-% CaO). Additionally, calcitic carbonate samples (>50 wt-% CaO) of BH-1 were analyzed (340, 488, and 670). Samples 488 and 670 have Fe concentrations of 388 and 514 $\mu g\ g^{-1}$ and δ^{56}Fe values of −0.878 and −0.558 permil, respectively, which are isotopically in the same range as the dolomitized samples. Sample 340 is a pure carbonate, contains 4415 $\mu g\ g^{-1}$ Fe, shows a lighter isotope signature of −1.819 permil, and is from the Gamohaan Formation, which was deposited during drowning of the CMCP.

The Kuruman Kop outcrop samples (table 3) encompass a range of δ^{56}Fe values from −1.744 to +0.453 permil and Fe concentrations between 463 and 12058 $\mu g\ g^{-1}$. Two samples from the Kogelbeen (Ku12/31) and the lowermost Gamohaan (Ku12/25) formations are detritus-free (fenestrate) limestones, which were deposited under lagoonal conditions (Sumner, 2002) and yield isotope values of −0.955 and −0.695 permil and Fe concentrations of 463 and 1076 $\mu g\ g^{-1}$, respectively. The other three samples are further up in the sequence of the Gamohaan and show variable values. Sample Ku12/26 is a detritus-poor Fe-rich dolomite (12058 $\mu g\ g^{-1}$, −0.289 ‰), whereas Ku12/06 yields δ^{56}Fe values of −1.744 permil and moderate Fe values of 3225

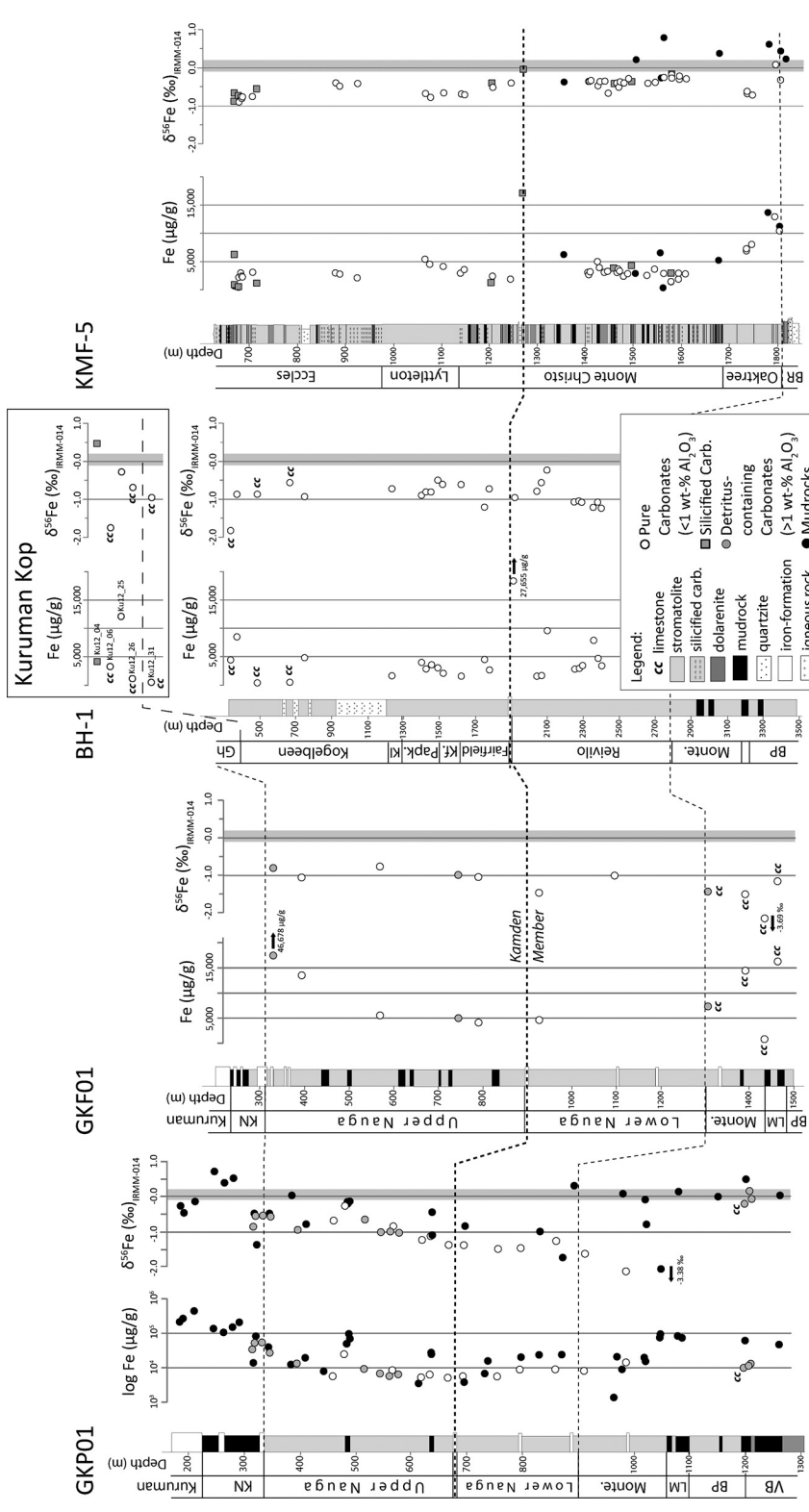

Fig. 3. Fe concentrations and isotopic compositions of carbonates and mudrocks from KMF-5, BH-1, Kuruman Kop (shelf succession), GKP01, and GKF01 [slope succession (Czaja and others, 2012)]. Shaded area at δ^{56}Fe columns indicates the range of continental signatures from −0.1 to +0.2 ‰ (for example Weyer and others, 2005; Schoenberg and von Blanckenburg, 2006; Craddock and others, 2013; Wang and others, 2014). Dashed black line shows stratigraphical relation of formations that belong to the Campbellrand-Malmani slope-shelf succession. The thicker dashed line indicates the Kamden Member. Abbreviations of formations: VB: Vryburg; BP: Boomplaas; LM: Lokamonna; Monte.: Monteville; KN: Klein Naute; Kf.: Klipfonteinheuwel; Papk.: Papkuil; Kl: Klippan; Gh: Gamohaan; BR: Black Reef.

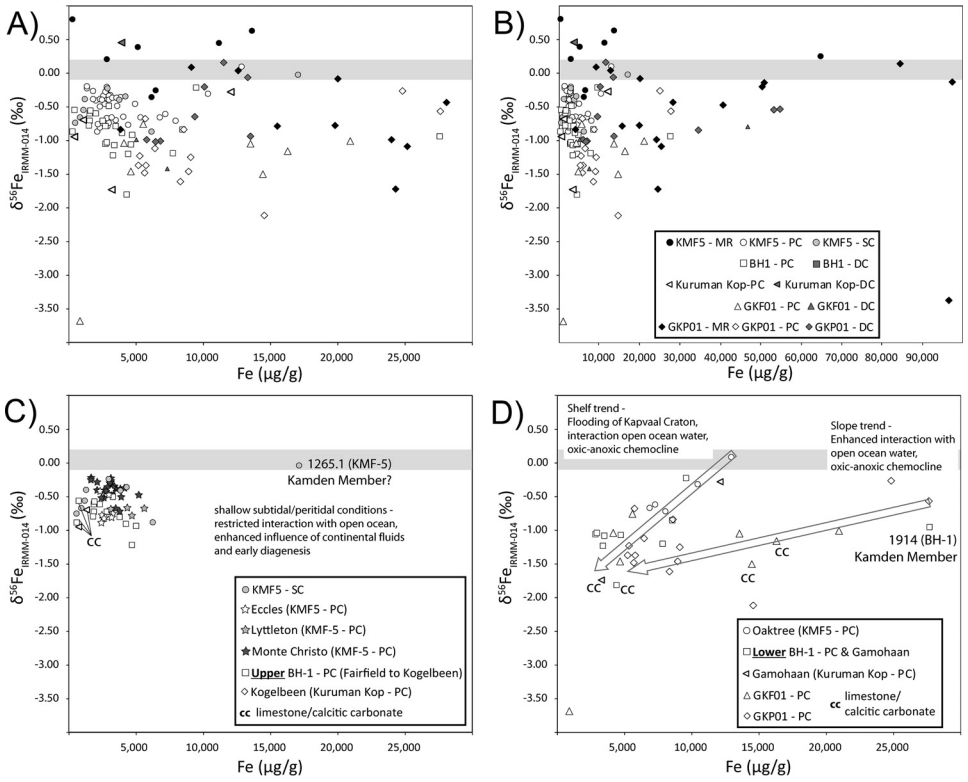

Fig. 4. δ^{56}Fe signatures vs. Fe concentrations of pure (PC), silicified (SC), and detritus-rich (DC) carbonates and mudrock samples from slope (GKP01, GKF01) and shelf (BH-1, KMF-5, Kuruman Kop) successions analyzed throughout the stratigraphy and highlighted into groups. Gray bar indicates the isotopic range of igneous rocks. (A) Plot of samples up to a concentration of 30,000 µg g^{-1} Fe. (B) Plot of samples up to a concentration of 100,000 µg g^{-1} Fe. (C) Carbonate samples deposited under lagoonal conditions, restricted interaction with open ocean water, and enhanced influence of continental fluids. δ^{56}Fe signatures in carbonates of the Monte Christo Formation are relatively heavy and probably reflect remobilization of Fe from adjacent pyrite-containing and isotopically heavy mudrocks. (D) Carbonate samples deposited under open ocean water conditions show depth-depending trendlines. Trendline 'Shelf' represent carbonates from the Oaktree, Reivilo and Gamohaan formations and trendline 'Slope' carbonates from the slope succession. Both were exposed to ferruginous open ocean water. Both trendlines show a positive correlation between Fe isotopes and Fe content, which probably reflects Rayleigh fractionation processes during oxidation of $Fe(II)_{aq}$ and deposition of isotopically heavy $Fe(III)_{ppt}$.

µg g^{-1}. Ku12/04 is a clay-rich chert, which was deposited within a siderite-rich mudrock interval and shows heavy signatures of +0.453 permil and a Fe concentration of 4031 µg g^{-1}.

Synchrotron-based X-ray Absorption Spectroscopy

For the statistical evaluation of the XANES, the number of unique mineralogical components represented by the collection of XANES spectra was determined using the 'principle component analysis' (PCA) tool from PyMCA. Table 4 shows the variance of the first five principle components (PC01 – PC05), the percentage indicates the significance of the respective PC. According to that, all samples are represented by two to three distinct mineralogical components. A 'linear combination fitting' of the composite, which is an average spectrum from each sample, was performed with the Athena software package (Ravel and Newville, 2005), using the number of components

TABLE 1

Iron concentration and isotope values of carbonate and mudrock samples of KMF-5

Depth (m)	Lith.	XRF analyses							MC-ICP-MS analyses				
		SiO_2 (wt-%)	CaO (wt-%)	MgO (wt-%)	Al_2O_3 (wt-%)	MnO (wt-%)	Fe_2O_3 (wt-%)	Fe#	Fe ($\mu g\ g^{-1}$)	$\delta^{56}Fe$ (‰)	2σ SE	$\delta^{57}Fe$ (‰)	2σ SE
Eccles													
665.08	SC	4.60	30.33	19.70	bdl	0.62	0.93	0.58	6270	-0.883	0.044	-1.127	0.095
665.18	SC	81.59	5.41	3.72	bdl	0.10	0.26	0.70	922	-0.665	0.044	-1.016	0.085
673.84	SC	86.76	3.64	2.58	bdl	0.07	0.17	0.69	580	-0.746	0.044	-1.119	0.083
674.55	PC	1.37	30.71	20.72	0.16	0.42	0.38	0.45	2211	-0.877	0.046	-1.304	0.083
678.60	PC	0.22	31.88	20.99	bdl	0.48	0.52	0.49	2997	-0.802	0.049	-1.156	0.079
680.58	PC	0.53	30.94	20.94	0.03	0.42	0.40	0.46	2436	-0.824	0.040	-1.248	0.079
682.70	PC	2.36	30.36	20.62	bdl	0.43	0.42	0.47	2275	-0.769	0.035	-1.143	0.065
703.30	PC	2.65	30.70	20.36	0.07	0.44	0.48	0.50	3106	-0.747	0.041	-1.107	0.073
711.80	SC	72.89	8.12	5.61	0.02	0.14	0.24	0.61	1203	-0.554	0.045	-0.850	0.076
875.50	PC	0.68	31.02	20.87	bdl	0.53	0.47	0.44	2990	-0.399	0.051	-0.637	0.081
884.83	PC	2.92	30.93	20.32	0.29	0.49	0.45	0.45	2789	-0.470	0.040	-0.706	0.086
921.78	PC	1.06	30.89	20.86	bdl	0.45	0.43	0.46	2123	-0.412	0.032	-0.604	0.069
Lyttleton													
1062.50	PC	0.39	31.42	20.29	0.06	1.13	0.82	0.40	5413	-0.673	0.034	-0.980	0.065
1072.73	PC	0.44	31.59	20.56	0.01	0.91	0.68	0.40	4534	-0.775	0.043	-1.136	0.066
1100.20	PC	0.35	31.24	20.56	0.07	0.99	0.68	0.38	4138	-0.658	0.036	-0.970	0.067
1136.75	PC	0.98	31.12	20.70	0.17	0.59	0.48	0.42	2945	-0.681	0.033	-0.987	0.074
Monte Christo													
1143.70	PC	1.04	30.77	21.06	bdl	0.60	0.57	0.46	3595	-0.707	0.046	-1.039	0.079
1199.50	SC	81.22	5.48	3.82	0.14	0.10	0.28	0.72	1279	-0.401	0.044	-0.632	0.083
1202.58	PC	1.48	30.70	21.09	bdl	0.37	0.45	0.52	2422	-0.511	0.048	-0.752	0.087
1239.98	PC	1.71	30.65	20.80	bdl	0.33	0.36	0.50	1885	-0.398	0.048	-0.603	0.083
1265.10	SC	54.60	6.82	5.02	11.73	0.14	10.34	0.99	17148	-0.036	0.034	-0.033	0.070
1350.90	MR	48.89	0.18	2.21	27.34	0.01	0.95	0.99	6250	-0.366	0.042	-0.522	0.077

TABLE 1
(continued)

Depth (m)	Lith.	XRF analyses							MC-ICP-MS analyses				
		SiO_2 (wt-%)	CaO (wt-%)	MgO (wt-%)	Al_2O_3 (wt-%)	MnO (wt-%)	Fe_2O_3 (wt-%)	Fe#	Fe (μg g^{-1})	$\delta^{56}Fe$ (‰)	2σ SE	$\delta^{57}Fe$ (‰)	2σ SE
Monte Christo													
1401.00	PC	0.18	31.00	21.38	bdl	0.44	0.53	0.52	3084	-0.354	0.044	-0.567	0.082
1403.80	PC	1.16	30.69	21.24	bdl	0.35	0.50	0.56	2677	-0.348	0.035	-0.518	0.058
1406.80	PC	1.28	30.76	21.04	bdl	0.40	0.57	0.56	3188	-0.334	0.040	-0.500	0.071
1420.90	PC	1.40	30.47	20.84	0.11	0.55	0.83	0.58	5009	-0.464	0.048	-0.742	0.076
1425.40	PC	1.01	30.77	21.06	bdl	0.46	0.64	0.56	3935	-0.361	0.040	-0.507	0.068
1435.25	PC	1.09	30.73	21.12	0.08	0.37	0.50	0.55	3099	-0.350	0.047	-0.584	0.092
1442.17	PC	0.93	30.76	20.88	bdl	0.59	0.56	0.46	3289	-0.664	0.044	-1.025	0.085
1454.61	SC	5.53	28.62	19.95	bdl	0.41	0.61	0.57	3848	-0.411	0.045	-0.680	0.081
1461.80	PC	2.13	30.38	20.65	0.18	0.54	0.51	0.46	3078	-0.408	0.036	-0.650	0.075
1464.30	PC	1.04	30.77	20.92	bdl	0.54	0.70	0.54	3675	-0.500	0.039	-0.750	0.074
1467.10	PC	1.21	30.58	21.14	0.01	0.44	0.54	0.53	3340	-0.372	0.039	-0.595	0.076
1475.35	PC	3.19	30.16	20.38	0.39	0.53	0.42	0.42	2398	-0.398	0.043	-0.629	0.078
1484.80	PC	1.69	30.44	20.76	0.39	0.59	0.49	0.43	2873	-0.280	0.038	-0.409	0.065
1491.85	SC	4.40	29.53	20.46	bdl	0.46	0.69	0.58	4315	-0.351	0.038	-0.561	0.078
1499.85	MR	57.59	0.44	2.14	20.82	0.01	0.49	0.98	2904	0.201	0.047	0.317	0.084
1524.70	PC	0.80	30.70	21.32	bdl	0.42	0.45	0.49	2568	-0.406	0.037	-0.570	0.065
1539.90	PC	1.89	27.93	20.59	0.25	0.62	0.58	0.46	3658	-0.378	0.041	-0.544	0.079
1551.70	MR	64.19	0.08	1.70	18.71	0.01	1.02	0.99	6544	-0.269	0.048	-0.403	0.078
1557.70	MR	75.66	0.07	1.15	11.04	0.01	0.36	0.97	366	0.788	0.048	1.136	0.078
1558.88	PC	3.26	29.97	20.59	bdl	0.45	0.55	0.52	2907	-0.253	0.041	-0.342	0.080
1574.15	PC	0.95	30.68	21.44	0.03	0.35	0.32	0.45	1422	-0.232	0.040	-0.335	0.085
1574.25	PC	2.67	30.32	20.97	0.06	0.36	0.31	0.44	1470	-0.204	0.052	-0.292	0.089
1574.30	SC	11.22	27.20	19.01	0.03	0.33	0.52	0.59	2969	-0.235	0.045	-0.342	0.083
1589.75	PC	0.56	30.88	21.47	0.01	0.38	0.38	0.47	1884	-0.271	0.044	-0.404	0.081
1589.90	PC	2.08	30.25	21.15	bdl	0.37	0.52	0.56	2941	-0.219	0.044	-0.337	0.081
1604.60	PC	0.32	31.34	21.13	bdl	0.45	0.44	0.47	2821	-0.282	0.032	-0.449	0.068
1673.30	MR	85.12	0.86	1.12	4.89	0.02	0.85	0.97	5223	0.378	0.049	0.541	0.079

TABLE 1
(continued)

Depth (m)	Lith.	XRF analyses							MC-ICP-MS analyses				
		SiO_2 (wt-%)	CaO (wt-%)	MgO (wt-%)	Al_2O_3 (wt-%)	MnO (wt-%)	Fe_2O_3 (wt-%)	Fe#	Fe ($\mu g\ g^{-1}$)	$\delta^{56}Fe$ (‰)	2σ SE	$\delta^{57}Fe$ (‰)	2σ SE
Oaktree													
1731.10	PC	0.58	30.77	20.26	bdl	1.36	0.97	0.39	6884	-0.668	0.034	-0.976	0.070
1731.30	PC	0.61	30.76	20.22	bdl	1.31	1.03	0.42	7268	-0.616	0.037	-0.878	0.066
1742.30	PC	1.20	30.75	19.44	bdl	2.26	1.16	0.32	8028	-0.718	0.040	-1.035	0.064
1776.00	MR	57.72	0.14	3.02	19.44	0.01	2.03	0.99	13687	0.617	0.044	0.940	0.085
1790.10	PC	2.86	29.37	19.23	0.62	0.84	2.00	0.68	12941	0.083	0.044	0.048	0.085
1800.10	PC	1.53	31.53	19.68	0.46	0.98	1.56	0.59	10433	-0.318	0.043	-0.506	0.073
1800.30	MR	58.61	0.72	3.46	19.61	0.03	1.83	0.98	11244	0.440	0.046	0.635	0.080
1811.20	MR	48.99	2.14	6.65	16.78	0.15	9.20	0.98	65032	0.240	0.043	0.364	0.075

Major element data were analyzed by XRF and are from Eroglu and others, 2015. Lith.: Lithology, PC: 'pure' carbonate, SC: silicified carbonate, MR: mudrock. Extern reproducibility for $\delta^{56}Fe$ is ± 0.06 ‰ (2σ). bdl: below detection limit. Fe-Mn ratio: Fe# = Fe/(Fe+Mn).

TABLE 2

Iron concentration and isotope values of carbonate samples of BH-1

Depth (m)	Lith.	XRF analyses							MC-ICP-MS analyses				
		SiO_2 (wt-%)	CaO (wt-%)	MgO (wt-%)	Al_2O_3 (wt-%)	MnO (wt-%)	Fe_2O_3 (wt-%)	Fe#	Fe (µg g^{-1})	δ^{56}Fe (‰)	2σ	δ^{57}Fe (‰)	2σ
Gamohaan													
340	PC	4.87	50.21	0.93	0.93	1.04	1.10	0.49	4415	-1.819	0.040	-2.650	0.066
375	PC	1.50	30.60	18.95	0.33	0.99	1.44	0.57	8526	-0.854	0.040	-1.264	0.070
Kogelbeen													
488	PC	0.15	55.56	0.31	bdl	0.44	0.19	0.27	388	-0.878	0.051	-0.621	0.091
670	PC	1.46	53.40	1.61	bdl	0.41	0.24	0.34	514	-0.558	0.043	-0.814	0.074
751	PC	3.17	29.56	20.17	bdl	0.84	0.83	0.47	4834	-0.926	0.038	-1.359	0.077
Klippan													
1235	PC	0.69	31.26	20.44	bdl	0.63	0.36	0.34	1629	-0.721	0.043	-1.068	0.076
Papkuil													
1400	PC	0.90	30.09	20.42	0.10	0.99	0.74	0.40	4035	-0.897	0.049	-1.248	0.081
1425	PC	3.32	29.97	19.78	0.06	0.60	0.53	0.44	2832	-0.803	0.044	-1.195	0.065
1455	PC	3.03	29.49	19.95	0.31	0.84	0.63	0.40	3574	-0.804	0.038	-1.194	0.073
1490	PC	1.59	30.00	20.51	0.01	0.82	0.47	0.34	3075	-0.498	0.037	-0.779	0.088
Klipfonteinheuwel													
1520	PC	0.53	30.38	20.88	0.00	0.71	0.74	0.40	2105	-0.604	0.044	-0.882	0.079
Fairfield													
1620	PC	0.88	30.38	20.92	0.01	0.51	0.35	0.38	1667	-0.604	0.042	-0.912	0.082
1750	PC	2.81	29.54	19.29	0.60	1.29	0.78	0.35	4491	-1.207	0.044	-1.817	0.083
1776	PC	1.83	30.10	20.53	bdl	0.60	0.52	0.42	2645	-0.721	0.045	-1.096	0.075
Kamden													
1920	PC	3.73	28.75	17.30	bdl	1.73	3.64	0.65	27655	-0.951	0.044	-1.325	0.080
Reivilo													
2041	PC	0.56	30.71	21.05	bdl	1.03	0.29	0.20	1582	-0.790	0.030	-1.190	0.065
2066	PC								1686	-0.570	0.041	-0.850	0.074
2098	PC	0.39	30.80	20.62	0.03	1.65	0.30	0.14	9546	-0.225	0.030	-0.355	0.075
2250	PC	0.26	30.88	20.80	bdl	1.20	0.30	0.27	2818	-1.065	0.035	-1.570	0.060
2275	PC	0.63	30.86	21.09	bdl	1.07	0.57	0.33	2931	-1.037	0.042	-1.547	0.072
2293	PC	0.57	30.58	19.60	0.03	2.82	0.67	0.18	3475	-1.080	0.040	-1.625	0.075
2355	PC	0.81	30.61	18.52	0.04	3.54	1.23	0.24	7841	-1.204	0.036	-1.851	0.071
2379	PC	0.57	30.58	19.60	0.03	2.82	0.67	0.18	4720	-1.068	0.035	-1.608	0.072
2400	PC	0.27	31.03	20.56	bdl	1.64	0.50	0.22	3398	-1.235	0.035	-1.805	0.075

Major element data were analyzed by XRF and are partly from Eroglu and others (2015). Lith.: Lithology, PC: 'pure' carbonate. External reproducibility for δ^{56}Fe is ± 0.06 ‰ (2σ). bdl: below detection limit. Fe-Mn ratio: Fe# = Fe/(Fe+Mn).

TABLE 3

Iron concentration and isotope values of carbonate samples of the Kuruman Kop outcrop

Sample	Location		Lithology	XRF-Analyses							MC-ICP-MS analyses				
	m.a.s.l. (m)	GPS data		SiO_2 (wt-%)	CaO (wt-%)	MgO (wt-%)	Al_2O_3 (wt-%)	MnO (wt-%)	Fe_2O_3 (wt-%)	Fe#	Fe (µg g^{-1})	$\delta^{56}Fe$ (‰)	2σ	$\delta^{57}Fe$ (‰)	2σ
Gamohaan															
KU 12/04	1483	S27°23'00.2'' E23°20'43.2''	MR (silicified siliciclastic horizon)	79.72	0.18	1.11	10.18	0.04	2.42	0.98	4031	0.453	0.042	0.645	0.089
KU 12/06	1478	S27°22'57.7'' E23°20'41.3''	PC (microbial mats)	1.53	53.67	0.54	0.27	1.06	0.54	0.32	3225	-1.744	0.057	-2.586	0.092
KU 12/26	1408	S27°22'54.3'' E23°20'43.3''	PC (dolostone intertidal)	1.14	30.73	19.67	0.13	0.97	1.68	0.61	12058	-0.289	0.042	-0.421	0.084
KU 12/25	1402	S27°22'51.8'' E23°20'43.0''	PC (limestone)	0.45	53.62	1.99	bdl	0.53	0.27	0.31	1076	-0.695	0.046	-1.015	0.082
Kogelbeen															
KU 12/31	1356	S27°22'50.7'' E23°20'37.0''	PC (fenestral carbonate)	0.12	55.46	0.50	bdl	0.45	0.12	0.19	463	-0.955	0.041	-1.374	0.085

Major element data were analyzed by XRF and are partly from Eroglu and others (2015). m.a.s.l.: meter above sea level. PC: 'pure' carbonate, MR: 'mudrock' Extern reproducibility for $\delta^{56}Fe$ is ± 0.06 ‰ (2σ). bdl: below detection limit. Fe-Mn ratio: Fe# = Fe/(Fe+Mn).

TABLE 4

XAS analyses, statistical evaluation and characterization of Fe species from KMF-5 and BH-1 carbonate and mudrock samples

Formation	Sample (Depth)	XAS Method	Remarks	map size (µm*µm)	pixel size (µm)	Fe-species (Absorption intensity; Marcus *et al.*, 2009)			Principle component analyses (variance, %)					Linear combination fitting - best fit				
						θ (eV) 7111.25	κ (eV) 7114.25	µ (eV) 7118.75	PC01	PC02	PC03	PC04	PC05	proportion amount of iron species				
KMF-5															total	R-factor	χ^2	χ^2 reduced
Eccles	665.08	Fluo	P-C	700x340	20x20	0.008	0.034	0.098	96.45	2.53	0.40	0.23	0.20	*goethite (0.846)* *siderite (0.139)*	0.99	0.0078	0.2568	0.0017
	665.18	Fluo	S-C	500x500	20x20	0.018	0.045	0.125	84.00	9.05	3.67	1.13	0.60	*goethite (0.649)* *siderite (0.124)* *ferrosmectite (0.233)*	1.01	0.0077	0.2543	0.0017
	884.9	Fluo	P-C	1000x1000	50x50	0.011	0.040	0.100	90.19	6.79	1.03	0.73	0.35	*goethite (0.603)* *ferrosmectite (0.438)*	1.04	0.0098	0.3681	0.0024
Lyttleton	1062.5	Trans	P-C	2000x2000	20x20	0.045	0.056	0.243	93.46	3.67	2.28	0.19	0.08	*ankerite (0.869)* *siderite (0.090)*	0.97	0.0015	0.1000	0.0003
	1100.3	Fluo	P-C	400x400	10x10	0.004	0.036	0.125	94.11	3.72	0.46	0.31	0.22	*ankerite (0.735)* *goethite (0.233)*	0.97	0.0128	0.4234	0.0027
Monte Christo	1265.2	Fluo	S-C (Fe-rich)	300x300	15x15	0.040	0.073	0.209	88.72	6.75	2.34	1.12	0.51	*chlorite (0.861)* *siderite (0.107)* *ferrosmectite (0.060)*	1.03	0.0017	0.0580	0.0004
	1524.7	Trans	P-C	2000x2000	20x20	0.056	0.068	0.219	92.81	4.44	1.08	0.47	0.29	*ankerite (0.939)* *siderite (0.059)*	1.00	0.0091	0.6506	0.0020
Oaktree	1742.3	Trans	P-C	2000x2000	20x20	0.024	0.041	0.221	94.76	3.36	1.31	0.12	0.07	*ankerite (0.909)* *siderite (0.071)*	0.98	0.0033	0.2323	0.0007
	1742.3	Trans	pyrite hotspots		20x20	0.046	0.103	0.457						*pyrite (0.658)* *siderite (0.296)* *ankerite(0.056)*	1.01	0.0072	0.3721	0.0011
	1776.0	Fluo	MR	700x700	23x23	0.041	0.122	0.567	84.64	9.60	3.73	0.93	0.21	*pyrite (0.945)* *magnetite (0.076)*	1.02	0.0012	0.0304	0.0002
BH-1																		
Gamohaan	340	Trans	D-C, calcitic	2000x1700	20x20	0.069	0.074	0.239	94.64	4.54	0.23	0.12	0.07	*ankerite (0.670)* *siderite (0.212)* *minor pyrite(0.037)*	0.92	0.0053	0.2883	0.0009
	340	Trans	pyrite hotspots		20x20	0.048	0.107	0.545						*pyrite(0.829)* *siderite (0.117)* *ankerite (0.066)*	1.01	0.0018	0.0930	0.0003
Reivilo	2540	Fluo	P-C	400x400	10x10	0.038	0.078	0.250	84.00	6.68	3.24	1.54	1.41	*ankerite (0.936)* *marcasite (0.079)* *magnetite (0.100)*	1.12	0.0051	0.2037	0.0013

R-factor: discrepancy index, the agreement between calculated and observed intensities; χ^2: 'Goodness of fit'-test, squared difference between calculated and observed data; χ^2 reduced: χ^2 divided by the number of degrees of freedom; Fluo: fluorescence method, Trans: transmission method; P-C: 'pure' carbonate, S-C: silicified carbonate, D-C: detritus-containing carbonate, MR: mudrock.

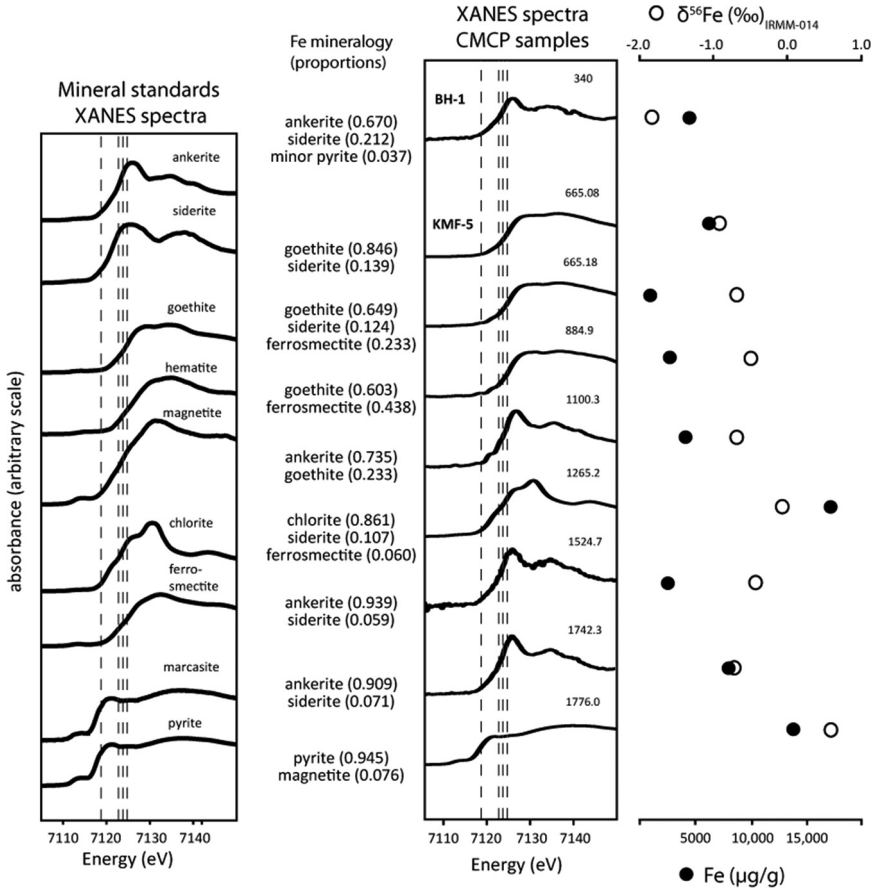

Fig. 5. XANES spectra of mineral standards and analyzed samples used to fit the sample spectra (see tables 4 and supplementary material for details, compositional reconstruction, and references). Different Fe mineral phases and characteristic edge-peak inflection point (vertical dashed lines) are from left to right (O'Day and others, 2004): Fe-sulfides, Fe carbonates, Fe-(hydr)oxides, and phyllosilicates. Calculated proportions of analyzed samples are given to their left. Note the change in the spectra from lower to upper part of CMCP carbonate rocks. Corresponding Fe concentrations and δ^{56}Fe signatures of samples are given to the right.

determined by PCA to guide the number of mineral standard spectra used to fit. The standard database consisted of spectra from ankerite, siderite, goethite, magnetite, pyrite, marcasite, chlorite and ferrosmectite (table SM-4; supplementary material, http://earth.geology.yale.edu/%7eajs/SupplementaryData/2018/Eroglu). The exact proportions are listed in table 4 and the corresponding linear fits are illustrated in figure 5 and the figures S1 a-d (Supplementary material, http://earth.geology.yale.edu/%7eajs/SupplementaryData/2018/Eroglu). The following samples, representing all lithologies and formations of the CMCP shelf, were analyzed from the KMF-5 and BH-1 drill cores: seven pure carbonates (665.08, 665.18, 884.9, 1062.5, 1100.3, 1524.7, 1742.3; KMF-5 and BH-1), one pure calcitic carbonate (340, BH-1), one silicified carbonate (665.18, KMF-5), one mudrock (1776.0, KMF-5) and one Fe- and silicate-rich carbonate (1265.2, KMF-5; fig. 5). Carbonates from the lower CMCP (Oaktree, Monte Christo, Reivilo formations; steep ramp architecture) predominantly show the coordination environment of Fe(II) mineral phases, mainly ankerite, with minor

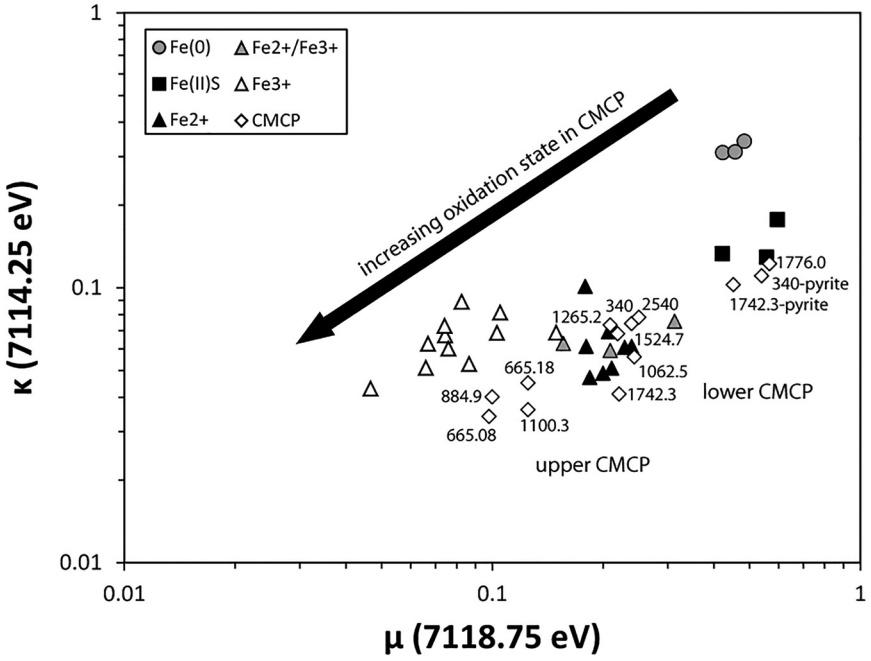

Fig. 6. Classification of distinct Fe (redox-)species analyzed by Marcus and others (2009), plotted based on their absorption at 7111.25 (θ), 7114.25(κ) and 7118.75(μ). Data from composite spectra from samples of the CMCP show that with continuing growth of the platform, the Fe oxidation state increased. See table 4 for details.

amounts of siderite, Fe sulfide (pyrite, marcasite), and mixed-valence Fe oxides (magnetite). The mudrock sample 1776.0 from the Oaktree Formation contains mainly pyrite with minor magnetite and the Fe- and silicate-rich sample 1265.2 (Kamden Member equivalent) consists mainly of chlorite with minor siderite and ferrosmectite. Towards the upper CMCP (Lyttleton, Eccles, Kogelbeen formations; rimmed margin architecture) this mineral composition significantly changes in favor of Fe(III) mineral phases, which best fit by the goethite standard (FeOOH) (figs. 5 and 6). The Lyttleton Formation carbonates consist mainly of ankerite, but show some admixture of goethite in the XANES spectra (1100.3). The carbonates of the Eccles Formation (665.08, 665.18 and 884.9) have significantly different spectra from the rest of the analyzed carbonates, containing mainly the Fe(III)-(oxyhydr)oxide goethite. Other components of Eccles samples are siderite and ferrosmectite (detailed amounts in table 4), whereas there is no sign of Fe-sulfide. Sample 340 (Gamohaan Formation, BH-5, GWA) shows mainly Fe(II)-carbonate signatures with minor amounts of pyrite that are visible as red "hotspots" in the XANES maps (fig. S1 d; supplementary material, http://earth.geology.yale.edu/%7eajs/SupplementaryData/2018/Eroglu).

As the pre-edge can also give valuable information about the oxidation state and speciation of Fe, a plot was constructed, based on the normalized absorption values θ, κ, and μ at defined energies (7110, 7113 and 7117.5 eV) (Marcus and others, 2009). As the Fe K-edge during the experiment was at 7112 eV, in contrast to the Fe K-edge of 7110.75 used by Marcus and others (2009), θ, κ, and μ values for the samples were defined at 7111.25, 7114.25 and 7118.75 eV, respectively, and compared to the θ, κ, and μ values defined for Fe(II), FeS, mixed valence, and Fe(III) mineral standards of Marcus and others (2009). The results are displayed in figure 6 and are consistent with

the presence of FeS, Fe(II), and Fe(III) phases within the dataset, and illustrate an increase in the Fe oxidation state towards the upper CMCP.

DISCUSSION

Early Diagenesis and Preservation of Geochemical Signatures

Diagenetic processes of different grades affected the CMCP, which mainly includes large-scale dolomitization as well as silicification in the peritidal environment, covering lower greenschist facies metamorphic conditions (Button, 1973; Eriksson and Truswell, 1973; Eriksson and others, 1975; Truswell and Eriksson, 1975; Eriksson, 1977; Beukes, 1987; Frauenstein and others, 2009). Contact-metamorphic overprint in the northeastern part of the TA due to the intrusion of the Bushveld complex even reached granulite-facies metamorphic conditions, however this did not affect samples analyzed here from KMF-5, which is in about 80 km distance to the contact zone (Frauenstein and others, 2009; Eroglu and others, 2017). Deciphering the impact of these diagenetic processes on the geochemical paleoproxies is crucial in order to correctly distinguish and interpret primary and secondary signatures (Brand and Veizer, 1980; Veizer, 1983; Banner, 1995). Nevertheless, the CMCP is one of the best preserved carbonate platforms of Neoarchean age, where sedimentological observations, like finely laminated stromatolitic structures, and geochemical signatures still allow a reconstruction of water depth, water circulation, and continental input (for example, Beukes, 1987; Altermann and Siegfried, 1997; Sumner and Beukes, 2006). Variations in Fe and Mn concentrations and Fe/Mn ratios of carbonates (expressed as $Fe\# = [Fe_{tot}/(Fe_{tot}+Mn_{tot})]$; fig. S2 a; supplementary material, http://earth.geology.yale.edu/%7eajs/SupplementaryData/2018/Eroglu), correlate to platform evolution, water depth and influx of hydrothermally influenced and continental waters, visible in REE+Y signatures (fig. S2 b; supplementary material, http://earth.geology.yale.edu/%7eajs/SupplementaryData/2018/Eroglu) (Beukes, 1987; Webb and Kamber, 2000; Voegelin and others, 2010; Eroglu and others, 2015; Eroglu and others, 2017). Carbonates deposited under (shallow) subtidal conditions during the steep-ramp architecture phase of the lower CMCP (for example, Reivilo, Oaktree formations) (fig. 2C) show Fe# values as a function of water depth, resulting from the lower redox potential of Fe compared to Mn (Beukes, 1987; Eroglu and others, 2017). Carbonates deposited during the rimmed-margin architectural phase and/or adjacent to siliciclastic mudrocks show elevated Fe# values that indicate (1) stronger influence of continental fluids and (2) localized Fe circulation between carbonates and adjacent mudrocks during diagenesis (Eroglu and others, 2015; Eroglu and others, 2017). Thereby, Fe would have been released to the porewater during leaching and dissolution of siliciclastics, sulphides, and oxyhydroxides in mudrocks and carbonates and exchanged between those phases (Veizer, 1983). Indeed, mudrocks of KMF-5 contain significantly lower amounts of Fe (<1.50 wt-% Fe) than the average continental crust [3.92 wt-%, Rudnick and Gao (2003)] and post-Archean Australian Shale [PAAS, 5.05 wt-% Fe, Taylor and MacLennan (1985)]. This points to Fe mobilization during early diagenesis within the sediment under anoxic, likely sulfidic conditions, as indicated by the presence of Fe(II)-sulfides (table 4). These observations are confirmed by REE+Y signatures, which show variations that are associated with influx of different water sources and early diagenetic processes in the sediment (Voegelin and others, 2010; Eroglu and others, 2017). Since large parts of the CMCP were dolomitized and some parts silicified, it is important to estimate their effect on Fe# and REE+Y signatures. Those processes clearly have an impact on the Ca, Mg, and Si contents. Furthermore, the ionic radii of Mg^{2+}, Fe^{2+}, and Mn^{2+} are very similar and preferentially incorporated during dolomitization (Reeder, 1983), suggesting that dolomitization would affect the Fe and Mn content (Veizer, 1983). Comparing limestone with dolomite

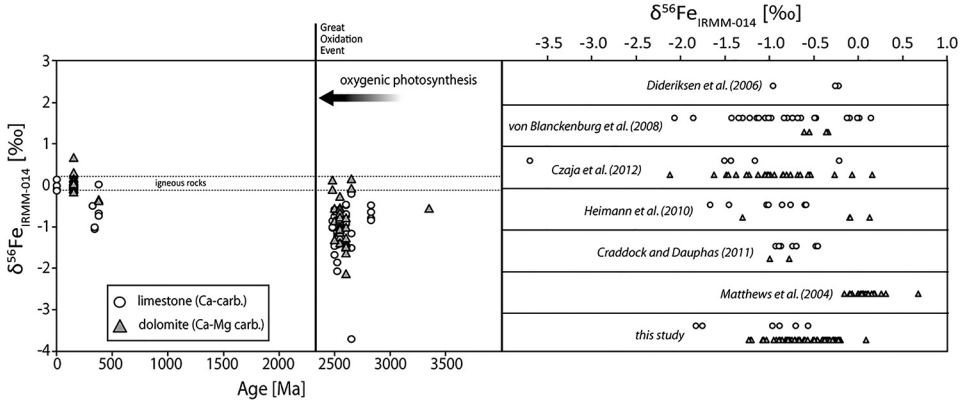

Fig. 7. Compilation of δ^{56}Fe isotope signatures [modified from Busigny and others (2014)], measured on Ca(-Mg) carbonates, highlighting the isotope signature of limestone and dolomite (Matthews and others, 2004; von Blanckenburg and others, 2008; Heimann and others, 2010; Craddock and Dauphas, 2011; Czaja and others, 2012).

shows that their Fe and Mn concentration ranges greatly overlap, although some limestones have lower Fe contents (tables 2 and 3). Importantly, the Fe and Mn contents still reflect the depositional conditions as described above and were not significantly overprinted by dolomitization. We therefore suggest that the Fe and Mn, which were incorporated into the carbonate structure during dolomitization, mainly comes from the original limestone, and therefore still reflects changes in water depth, platform architecture, water source, and fluid circulation during early diagenesis within the sediment (Eroglu and others, 2017). Silicification is a common observation in Precambrian carbonate platforms and in former near-shore sediments it is the result of mixing of marine and meteoric waters, which is favored by increasing porosity, salinity, and f_{CO2}, as well as decreasing pH (Knauth, 1979; Maliva and Siever, 1988, 1989; van den Boorn, ms, 2008). The silicified carbonates investigated here formed in that way (Eroglu and others, 2017) and overlap with pure carbonates in their Fe and Mn concentration range, with some strongly silicified samples showing lower concentrations than dolomites. The Fe and Mn content was probably diluted due to the incorporation of silica.

Fe isotope analyses reveal that there is no isotopic difference between calcitic and dolomitic samples (figs. 4C, 4D and 7; tables 1–3), which supports the study of von Blanckenburg and others (2008), showing that dolomitization has no effect on the δ^{56}Fe isotope composition of carbonate. To our knowledge, there is no experimentally determined fractionation factor for $Fe(II)_{aq}$ into Ca-Mg carbonates yet. However, dolomitization itself does not invoke a redox change, which means that a large Fe isotope fractionation is not expected (Schauble, 2004) and that any such fractionation must have been independent from dolomitization. Even though the δ^{56}Fe signatures seem to be unaffected by dolomitization, dolomitic samples have overall higher Fe concentrations than calcitic samples (figs. 4C and 4D). Therefore, even though dolomitization may not invoke a shift in the Fe isotope signature, it could cause a rise in the Fe content. However, this interpretation is undermined by some calcitic samples with Fe contents similar to dolomite, for example sample Ku12/06 (Gamohaan formation, Kuruman Kop) and samples from the slope facies (Czaja and others, 2012). Overall, calcitic and dolomitic carbonates can both be grouped according to their depositional environment. Similarly, silicified carbonates do not show a different isotope signature than peritidal unsilicified carbonates (fig. 4C). Since silicification

solely occurred in the peritidal environment, the Fe isotope composition and concentration was strongly impacted by continental fluids. Nevertheless, further investigations will be necessary to better understand the effect of dolomitization and silicification on the Fe systematics in Ca-Mg carbonates.

Mineralogy and Fe Speciation of CMCP Carbonates

Data from XAS analyses reveal major differences in the oxidation state of Fe incorporated in carbonates of the lower (steep ramp architecture) and upper (rimmed margin architecture) CMCP (figs. 5 and 6, table 4). Fe speciation was examined in XANES maps 1) in the matrix and 2) of discrete particles, which are visible as red "hotspots" in the edge jump maps that show the relative Fe concentration (fig. S1 a-d; supplementary material).

Carbonate samples consist of dolomite ($CaMg(CO_3)_2$), with minor calcite and silica, as is shown by the major element composition (tables 1–3) (Eroglu and others, 2015) and X-Ray diffraction (XRD) (fig. S3, supplementary material) (Eroglu and others, 2017). The dominant Fe component in the shelf succession of the lower CMCP (Oaktree, Monte Christo, and Reivilo formations) is Fe(II)-containing carbonate, in particular ankerite $Ca^{2+} \cdot (Mg^{2+}, Fe^{2+})\ (CO_3)_2$ (Chai and Navrotsky, 1996), which forms when Fe substitutes for Mg in the dolomite structure. It could not be detected by XRD, probably because it is below the detection limit of the method (0.1–0.5 wt-%), but it is still detectable spectroscopically. Ankerite is heterogeneously distributed in the samples (fig. S1 b-d; supplementary material, http://earth.geology.yale.edu/%7eajs/SupplementaryData/2018/Eroglu), and minor amounts of Fe(II)-sulfides, mainly pyrite or marcasite, are visible as discrete particles (red "hot spots") in the XANES maps (samples 1742.3 (KMF-5), 2540 (BH-1), fig. S1 c-d; supplementary material). Similar to secondary framboidal Fe-sulfide formation in some carbonates and mudrocks of the Malmani succession (fig. S4; supplementary material) (Eroglu and others, 2015), these particles likely formed secondarily as aggregates during diagenesis by the reaction of mobilized Fe(II) and dissolved sulfide species (Wilkin and Barnes, 1997). In summary, carbonates in the Oaktree, Monte Christo and Reivilo formations solely contain Fe(II) mineral phases. This changes towards the upper part of the CMCP (figs. 4 and 5), where the carbonates of the Lyttleton and Eccles formations contain Fe(III) mineral phases. While the minor Fe phase in the Lyttleton Formation they become the dominant Fe phase in the Eccles Formation (table 4). XANES spectra best fit by goethite, however it is important to note that goethite could not be detected by XRD, which means that it is below its detection limit (fig. S3; supplementary material). Ankerite is still the major Fe phase in the Lyttleton Formation, but is no longer a component in the Eccles Formation, where instead traces of siderite and ferrosmectite are present. Neither in the Lyttleton nor in the Eccles formations is Fe(II)-sulfide present, which implies insufficient organic material to drive DIR and microbial sulfate reduction (MSR) in the sediment. The scarcity of organic-rich mudrocks and presence of Fe(III) oxides in the Eccles Formation supports this (Eroglu and others, 2015). Also, the few organic carbon rich mudrocks of the Eccles Formation lack framboidal pyrite, in contrast to the Fe-sulfide and organic carbon rich mudrocks of the Oaktree and the Monte Christo formation (Eroglu and others, 2015). This indicates that the lower CMCP had more reducing conditions and the upper CMCP more oxidizing conditions, which did not favor the formation of pyrites. In the samples of the upper CMCP, matrix and red "hotspots" do not show any differences in the mineralogy from the matrix. We conclude that 1) pyrite forms discrete particles in the lower CMCP, 2) ankerite is in the carbonate matrix of the lower CMCP, and 3) Fe(III) mineral phases are preserved in the carbonate matrix of the upper CMCP. Discrete Fe(III) particles were not observable using polarized light microscopy, indicating that the Fe(III) phases are finely distributed within the carbonate structure.

Preservation of Fe(III) mineral phases in the upper CMCP.—The characteristic edge-peak inflection points of XANES spectra (figs. 5 and 6) from the Lyttleton and Eccles formations clearly show a Fe(III) mineral phase. Although the best fit is by goethite, it is not absolutely certain that this Fe(III) phase is goethite or another Fe(III)-(oxyhyr)oxide (that is, hematite) without further spectroscopic or paleomagnetic analyses (de Kock and others, 2009), which however goes beyond the scope of this study.

Major and trace element data of the CMCP showed that the carbonates investigated here were not subject to fluid alteration by the Bushveld complex (Eroglu and others, 2015), which excludes a formation of Fe(III) phases by magmatic fluids in the analyzed samples. There is furthermore no ready explanation for dolomitization and silicification processes that would form goethite in the upper part of the CMCP but not in the lower part. A detrital input of goethite to the upper CMCP is possible, however the analyzed samples (665.08, 665.18, and 884.9) are pure carbonates with a negligible detrital component (table 4). XAS maps of the edge positions show that goethite is finely distributed in the carbonate structure and did not form to discrete particles as is observed for secondary Fe(II)-sulfides (fig. S1 a-d; supplementary material, http://earth.geology.yale.edu/%7eajs/SupplementaryData/2018/Eroglu), which argues against a secondary formation of goethite. Furthermore, detrital material rather consists of phyllosilicates such as chlorite and ferrosmectite, based on the XAS spectrum of detritus-containing sample 1265.1 (table 4).

Following these observations, we propose that Fe(III) phases formed *in-situ* during the precipitation of CMCP carbonates. An experimental study of Mettler (ms, 2002) and Mettler and others (2009) investigated the adsorption of Fe(II) cations on calcite surfaces. According to their model, Fe(II) is adsorbed onto the surface of calcite, forming reactive Fe(II) species ($>CO_3FeCO_3H^0$). This is under anoxic conditions considered as precursor for the formation of $Fe/CaCO_3$ precipitates and the incorporation of Fe into the crystal with a relative molar ratio of ~0.4 percent (Dromgoole and Walter, 1990; Mettler, ms, 2002). Under oxic conditions $>CO_3FeCO_3H^0$ is likely oxidized, forming Fe(III)-oxides. Hereby, under bicarbonate-rich, circumneutral conditions goethite is the preferably formed Fe(III)-phase (Schwertmann and Cornell, 2000; Cornell and Schwertmann, 2003). Although we cannot exclude that goethite is formed first and then precipitated and incorporated into the carbonate, we suggest to follow the model of Mettler (ms, 2002) and Mettler and others (2009), since it is supported by μXANES-maps of the here analyzed samples from Eccles and Lyttleton formations that show that Fe(III)-(oxyhydr)oxides are part of the carbonate matrix without forming any discrete particles. A study by van der Zee and others (2003) describes the formation of goethite in calcite-rich marine sediments and proposes that diagenetic goethite is the main reactive Fe phase that precipitates at oxic-anoxic boundaries in aquatic sediments. The nano-scale grain size (~12 nm) of goethite in the study of van der Zee and others (2003) explains why it is only detectable by spectroscopic methods. A possible scenario for Fe(III) mineral formation in microbialites of the CMCP could therefore be the adsorption of $Fe(II)_{aq}$ on calcite and oxidation to $Fe(III)_{ppt}$ by photosynthetically produced oxygen. Nevertheless, this scenario is speculative and the role of Fe oxidation on calcite requires further investigation. Furthermore, additional spectroscopic and paleomagnetic studies are necessary to carefully define the Fe(III) mineral phase.

The stratigraphical equivalent of the Lyttleton and the Eccles formations in the TA is the Upper Nauga Formation in the GWA, which represents the slope succession and, in contrast to the Lyttleton and Eccles formations, does contain Fe(II)-sulfides (Czaja and others, 2012). Based on the Fe-speciation data, the lower CMCP and the slope succession were too reducing, while conditions in the lagoonal interior during

the rimmed margin architecture stage (the upper CMCP) allowed for the preservation of Fe(III)-(oxyhydr)oxides (figs. 2C, 5 and 6). Preservation of Fe(III) phases implies that the organic carbon content in the upper CMCP was too low to drive diagenetic reduction of the Fe(III)-(oxyhydr)oxides (Froelich and others, 1979; Berner, 1981). In contrast, the more organic-rich lower CMCP fueled MSR and reductive dissolution of Fe(III)-(oxyhydr)oxides, forming $Fe(II)_{aq}$ that was subsequently incorporated into carbonates and sulfides. Another reason could have been the more intense interaction of the slope carbonates and shelf carbonates of the lower CMCP (steep ramp architecture) with open ocean water that was hydrothermally influenced, while the lagoonal interior was protected by the rimmed margin. The presence of Fe(III)-(oxyhydr)oxides in the upper part of the CMCP argue for this increasing oxidation state in the shallow marine environment and emphasize the dependence of this redox evolution on the platform architecture, as well as the balance of hydrothermal vs. continental input. The redox conditions probably changed again in the last stage of platform deposition, as the carbonate sample analyzed from the Gamohaan Formation (340, BH-1), deposited during the final drowning of the CMCP and contains mainly ankerite and minor siderite and pyrite (table 4). This change in mineralogy indicates a shift to reducing conditions due to a stronger interaction with the open ocean.

Fe Isotope Geochemistry of the CMCP

The Fe isotope and concentration data of samples analyzed throughout the stratigraphy of slope (GKP01, GKF01) and shelf (BH-1, KMF-5, Kuruman Kop) successions are highlighted in figures 4A–4D. Ca-Mg carbonates of slope and shelf successions consistently show δ^{56}Fe signatures lighter than the igneous rock range, with one exception in the lower Oaktree Formation (1790.1, δ^{56}Fe of +0.083 ‰, table 1). When plotting δ^{56}Fe signatures vs. Fe concentrations of pure carbonates, some dependences on the depositional environment and water depth become apparent (figs. 4C and 4D).

Effect of early diagenesis on the δ^{56}Fe signatures of Ca-Mg carbonates.—A cluster of carbonate samples show a restricted range of Fe concentrations below 5000 $\mu g\ g^{-1}$ and δ^{56}Fe compositions between about −0.2 and −1.0 permil (fig. 4C). Those samples represent peritidal settings (for example, Monte Christo and Eccles formations) and/or were deposited within the rimmed platform architecture [Lyttleton Formation (KMF-5); Fairfield to Kogelbeen formations (BH-1 and Kuruman Kop)]. The shallow-marine conditions under which they were deposited had restricted exchange with open ocean water and exposure to continental fluids, which is supported by elevated Fe# values and REE+Y signatures (figs. 2a-b, supplementary material; Eroglu and others, 2017). The circulation of porefluids in marine benthic sediments is an essential aspect in early diagenetic processes, and the source of these fluids is not only from sea- and freshwater, but also from dewatering processes within the sediment. Associated redox processes and changes in Fe speciation within the bulk sediment, microbial processes, as well as fresh- and seawater mixing can impact the fractionation of Fe isotopes (Beard and others, 2003a; Butler and others, 2005; Severmann and others, 2006; Rouxel and others, 2008; Préat and others, 2011). Additionally, interaction between carbonates and mudrocks likely played a role.

Mudrocks from the shelf (KMF-5) record heavier δ^{56}Fe signatures (mean with 2σ: +0.253 ± 0.803 ‰; n = 8) than the typical Fe isotopic composition of igneous rocks with signatures between −0.1 and +0.2 permil (for example Weyer and others, 2005; Schoenberg and von Blanckenburg, 2006; Craddock and others, 2013; Wang and others, 2014). This is in contrast to mudrocks from the slope succession of the CMCP (Boomplaas, Lokammona, Monteville, lower and upper Nauga - GKP01), which show overall lighter δ^{56}Fe signatures (-0.671 ± 1.807 ‰; n = 21) than igneous rocks (Czaja and others, 2012) (figs. 4A and 4B). The Fe inventory and isotope composition of the

mudrock layers from shelf and slope is dominated by Fe(II)-sulfides as shown by XANES (this study) and XRD (Czaja and others, 2012) analyses. Severmann and others (2008) postulated that a benthic Fe cycling affected sediments along Late Archean continental margins, similar to modern shelf-to-basin Fe shuttles (Lyons and Severmann, 2006; Severmann and others, 2006; Severmann and others, 2010). In this model, incomplete reduction of reactive Fe(III) in shelf sediments releases isotopically light $Fe(II)_{aq}$, which is transported to and recycled in the slope sediment, leaving the residual Fe in the shelf sediment isotopically heavy (Severmann and others, 2006; Staubwasser and others, 2006; Severmann and others, 2008; Rouxel and others, 2008; Heimann and others, 2010). Fe(III) reduction is typically driven by DIR or abiotically by reductive dissolution mediated by MSR-produced sulfide in the sediment, whereby DIR mobilizes reduced $Fe(II)_{aq}$ and sulfide-reduction immobilizes it by fixation into Fe-sulfides (Raiswell and Canfield, 1998; Butler and others, 2005). Enhanced fluxes of organic carbon due to primary production along the shelf CMCP (Eroglu and others, 2017) probably induced anoxic conditions down to sulfate reduction. Indeed, the pyrite-containing mudrock layers of the Monte Christo and Oaktree formations contain up to 8.5 weight percent total organic carbon, which implies a reducing environment that mobilizes $Fe(II)_{aq}$ from the sediment and favors MSR and pyrite formation (Berner, 1981). Traces of magnetite found in one mudrock sample (1776.0, KMF-5) with a $\delta^{56}Fe$ signature of +0.617 permil, possibly formed secondarily in the sediment from residual Fe(III)-(oxyhydr)oxides and $Fe(II)_{aq}$, according to:

$$3Fe^{2+}_{aq} + 6OH^{-} + 6Fe(OH)_3 \rightarrow 3Fe_3O_4 + 12H_2O \qquad (5.1)$$

(Heimann and others, 2010). All these findings support a shelf-to basin Fe shuttle leading to isotopically heavy shelf sediments and isotopically light slope sediments in the CMCP.

Carbonates of the Monte Christo Formation show the heaviest $\delta^{56}Fe$ signatures (mean with 2σ: -0.382 ± 0.258 ‰; n = 22) when compared to other carbonates from the Upper CMCP (Lyttleton, Eccles, and Fairfield to Kogelbeen formations; -0.731 ± 0.363 ‰; n = 26) (fig. 4C). The Monte Christo Formation also contains abundant mudrock layers. A study on a carbonate succession from the Upper Jurassic (Kimmeridge Clay Formation, UK) reported that carbonates adjacent to isotopically light, organic- and pyrite-rich mudrocks also showed lighter Fe isotope compositions relative to mudrock-free carbonate layers in the same succession. They concluded that carbonates are locally affected by mudrocks in the course of diagenetic Fe circulation in the sediment (Matthews and others, 2004). Following these observations, we propose that the Fe isotope composition of carbonates in the Monte Christo Formation were affected by adjacent isotopically heavy mudrock layers due to porewater circulation during early diagenesis. Elevated Fe# values and REE + Y signatures of carbonates confirm this interpretation, as they show a resemblance to the siliciclastic mudrocks and imply a localized remobilization of Fe (figs. 2a-b, supplementary material). Carbonates in the Monte Christo Formation also contain traces of Fe(II)-sulfides, as indicated by XANES data (table 4). This indicates MSR could have formed aqueous sulfide species, which migrated via porewaters between adjacent mudrock and carbonate layers. This is supported by strongly varying $\delta^{98}Mo$ signatures (-0.82 to $+1.40$ ‰) in the lower CMCP shelf (Eroglu and others, 2015), which was likely influenced by the flux of dissolved sulfide, organic matter, and Fe-oxides that scavenge and remobilize Mo during early diagenesis within the sediment (for example McManus and others, 2006; Poulson and others, 2006; Siebert and others, 2006). All these observations can explain the heavy $\delta^{56}Fe$ signatures of carbonates in the Monte Christo Formation (fig. 4C), which were likely influenced by mobilized $Fe(II)_{aq}$ that migrated, like the aqueous sulfide species, via porewaters from isotopically heavy mudrocks.

Carbonate samples from the shelf succession of the Upper CMCP [Eccles, Lyttleton (KMF-5); Fairfiel to Kogelbeen (BH-1, Kuruman Kop)] have lighter isotope signatures than Monte Christo Formation carbonates. Still, Fe# values and REE+Y signatures imply a 'continental' influence on their Fe isotope composition. Due to the rimmed margin, the interior lagoon influx of open ocean water was restricted and freshwater from the continent had a greater impact on these carbonates. Riverine water has variable δ^{56}Fe signatures between about 0 and −1 permil (for example Beard and others, 2003b; Bergquist and Boyle, 2006) and could be reflected in the mean of -0.731 ± 0.363 permil of Upper CMCP shelf carbonates. Another influence on the Fe isotope signature could be due to goethite, being the best fit for Fe(III) mineral phases found in both the Eccles and Lyttleton formations, although further studies are necessary to confirm this finding. Beard and others (2010) experimentally determined under anoxic conditions at 20 °C an equilibrium fractionation between $Fe(II)_{aq}$ and goethite ($\Delta^{56}Fe_{Fe(II)aq\text{-}goethite}$) of -1.05 ± 0.08 permil, however they also show that adsorbed or surface Fe phases alter the overall signature. Polyakov and Mineev (2000) calculated an average theoretical $\Delta^{56}Fe_{Fe(II)aq\text{-}goethite}$ of around 0 permil. Dideriksen and others (2006) analyzed the Fe isotope signature of hydrothermal calcite and goethite and postulated a dependence on the aqueous Fe species. Thereby, the Fe isotope fractionation is negligible when siderite and goethite is formed in equilibrium with $Fe(II)_{aq}$, but is larger when formed in equilibrium with $Fe(III)_{aq}$, resulting in lighter δ^{56}Fe signatures of siderite and goethite. They propose that both, calcite and goethite, reflect the ambient fluid composition, when the dominant species is $Fe(II)_{aq}$, and not $Fe(III)_{aq}$. Although these studies are informative, a comprehensive experimental study on the Fe isotope fractionation in marine carbonates is lacking. In case of the Lyttleton and Eccles formations, there is no difference in their Fe isotope composition, even though the dominant Fe phase in Lyttleton carbonates is ankerite with only minor goethite, whereas Eccles mainly contains goethite. That either means that the fractionation of Fe isotopes during the formation of goethite was negligible or that goethite exchanged isotopically with $Fe(II)_{aq}$ in porewaters after its formation. It remains elusive how and if the change in Fe speciation from the lower CMCP to the upper CMCP had an effect on the isotope compositions of the carbonates, and to what extent early diagenesis overprinted the primary compositions.

Fe isotope systematics along an aqueous redox-boundary reflected in CMCP carbonates.—Beside the data cluster of carbonates deposited under peritidal and/or restricted conditions (fig. 4C), the dataset of Fe concentration vs. Fe isotope composition reveals two positively correlated trendlines ('Shelf' and 'Slope', fig. 4D). The 'Shelf'-trendline consists of samples from the Oaktree (KMF-5) and Reivilo formations (BH-1), which were deposited during the earlier steep platform stage and were exposed to open ocean water. Carbonates of the Oaktree Formation show a very good positive correlation ($R^2 = 0.93$) between Fe concentrations and δ^{56}Fe composition. Samples Ku12/06 and Ku12/25 (Kuruman Kop) and samples 340 and 375 (BH-1) from the Gamohaan Formation were deposited during the drowning of the CMCP and also fall on this 'Shelf' trend, likely reflecting their interaction with open ocean water. The 'Slope' trendline captures a shift to lighter isotope signatures with decreasing Fe concentration. It consists of samples from the slope facies (GKP01, GKF01), which were exposed to Fe-rich deep ocean water. Interestingly, sample 1914 from BH-1 also fits the 'Slope' trendline (fig. 4D). Considering that this pure carbonate was deposited coeval to the deposition of the Kamden Member, we suggest, that the intense influx of Fe-rich open ocean water is reflected in sample 1914. These observations are supported by the respective Fe# values and REE+Y signatures of these samples, reflecting open and shallow seawater (figs. 2a-b, supplementary material) (Voegelin and others, 2010; Eroglu and others, 2017). Overall, the Fe isotope composition of these 'trendline'-

carbonates was mainly influenced by processes involving interaction with open ocean water and a negligible continental impact, in contrast to the 'cluster'-carbonates that were mainly influenced by continental fluids and early diagenetic processes.

Oxidation of $Fe(II)_{aq}$ along a chemocline probably played an important role in the CMCP, as several studies indicate the presence of oxygen in the shallow ocean (Sumner and Grotzinger, 1996; Wille and others, 2007; Brucker and others, 2009; Godfrey and Falkowski, 2009; Kendall and others, 2010; Voegelin and others, 2010; Czaja and others, 2012). The appearance of minor Fe-rich layers, like the Kamden Member that formed in the course of a short transgressive event, shows the presence of coeval ferruginous deeper water (fig. 4D) (Sumner and Beukes, 2006; Beukes and Gutzmer, 2008). The oxidation of $Fe(II)_{aq}$ along a chemocline separating anoxic ferruginous deeper water from oxic shallow water and the subsequent precipitation of Fe(III)-(oxyhydr)oxides along this chemocline is a commonly cited scenario for the formation of some Precambrian IFs (for example Cloud, 1968; Holland, 1984; Isley and Abbott, 1999). Aerobic oxidation of $Fe(II)_{aq}$ to $Fe(III)_{ppt}$ causes an enrichment of heavy Fe isotopes in the precipitate by 1 to 2 permil (Bullen and others, 2001; Beard and others, 2003a). This is similar to anoxygenic photosynthetic microbial Fe(II) oxidation, which shows an enrichment of up to 2 permil (Croal and others, 2004; Swanner and others, 2015b). Either way, incomplete oxidation causes the remaining $Fe(II)_{aq}$ pool to become isotopically lighter, due to the separation of the precipitated Fe(III)-(oxyhydr)oxides from the reservoir of dissolved Fe(II) remaining in seawater (Rouxel and others, 2005). A study by Busigny and others (2014) examined whether the Fe cycle and resulting sedimentary Fe isotopic signatures in the ferruginous, redox-stratified meromictic Lac Pavin is influenced by water column redox chemistry or by benthic DIR. The Fe isotope composition of pyrite in the benthic environment along the chemocline is variable, but overall negative, and mirrors the Fe isotope composition of aqueous Fe. They concluded that Fe sulfide formation induces only a limited Fe isotope fractionation and that the observed isotope fractionation in the Lac Pavin setting is not connected to pyrite formation but to the Fe(II) oxidation within the water column. The implication is that the strong Fe isotope variability in Neoarchean Fe-minerals (fig. 1B) can rather be linked to partial ferrous Fe(II) oxidation in upwelling water masses (Kurzweil and others, 2016). Similarly, studies of Dideriksen and others (2006) and von Blanckenburg and others (2008) imply that calcite incorporates $Fe(II)_{aq}$ from the ambient fluid and reflects its isotope composition. Thus, a systematic Fe isotope variability of carbonates deposited under open ocean conditions, as shown in the 'Shelf' and 'Slope' trendlines can be explained by titration of Fe from seawater along a redox boundary between ferruginous deeper water, which was supplied via upwelling into oxygenated shallow seawater, resulting in a low Fe concentration and a lighter isotope signature of the remaining $Fe(II)_{aq}$ pool (Rouxel and others, 2005; Busigny and others, 2014). Depth-dependent Fe# values and respective REE+Y signatures support that these carbonates reflect open ocean signals.

Based on this interpretation, we hypothesized that data from these 'Shelf' and 'Slope' trendlines could be used to determine the initial $Fe(II)_{aq}$ concentration of the deep anoxic seawater that supplied the platform, as well as the fractionation factor α (converted to permil units via $\varepsilon = (\alpha - 1) \times 1000$) between $Fe(II)_{aq}$ and $Fe(III)_{ppt}$ by fitting the data with a Rayleigh distillation equation. In order to do this, it was necessary to plot $\delta^{56}Fe$ vs. Fe concentration of the 'Shelf' and 'Slope' trendline samples, while making some assumptions and conversions about how these values reflect coeval Fe in seawater. First, the $Fe(II)_{aq}$ concentration corresponding to each sample was based on the Fe concentration of the carbonates (table 5), and utilized the distribution factor D_{Fe2+} determined by precipitation experiments and Fe incorporation into calcite by

Dromgoole and Walter (1990). The distribution factor is mainly dependent on the temperature and precipitation rate, and is defined as:

$$D_{Fe^{2+}} = \frac{\frac{Fe^{2+}}{Ca^{2+}_{\text{calcite}}}}{\frac{a_{Fe^{2+}}}{a_{Ca^{2+}\text{solution}}}} \tag{5.2}$$

where $\frac{Fe^{2+}}{Ca^{2+}_{\text{calcite}}}$ is the molar ratio of Fe^{2+} and Ca^{2+} in the precipitated calcite and $\frac{a_{Fe^{2+}}}{a_{Ca^{2+}\text{solution}}}$ is the activity ratio of Fe^{2+} and Ca^{2+} in solution and is the product of the concentration and the activity ratio (Dromgoole and Walter, 1990). The activity coefficient γ_i depends on the ionic strength, concentration of the cation, and the cation charge, but was during the experiments of Dromgoole and Walter (1990) always close to unity. For the carbonates of this study, we used the equation from Dromgoole and Walter (1990) for precipitation experiments at 25 °C and an activity ratio $\frac{a_{Fe^{2+}}}{a_{Ca^{2+}}}$ of 0.001, which is in the magnitude that represents the here analyzed carbonates:

$$\log D_{Fe^{2+}} = 0.98 - 0.158 \times \log(rate) \tag{5.3}$$

where *rate* is the precipitation rate of the calcite. The precipitation rate was calculated from the assumed sedimentation rate along the slope (~10 m/Ma) and the shelf (~100 m/Ma) of the CMCP (Altermann and Nelson, 1998). Since the Fe# values of the samples show a depth-dependence, it was assumed that all Fe(II) in the samples was originally incorporated into calcite and did not change during dolomitization (Diderriksen and others, 2006; von Blanckenburg and others, 2008). Since Dromgoole and Walter (1990) used calcite for their experiments, we used a fixed $Ca^{2+}{}_{aq}$ concentration for dolomitized samples of 20 mM (Horita and others, 2002) to simulate a calcite composition (table 5).

Second, using data of 'Shelf' and 'Slope' trendlines, we calculated the fractionation factor α (expressed as $\varepsilon^{56}Fe(III)_{ppt}$-$Fe(II)_{aq}$) and $Fe(II)_{aq\text{-initial}}$, by comparing the fit to the $\delta^{56}Fe$ carbonate dataset and minimizing the sum of χ^2 values ($\Sigma\chi^2$). The fit was based on a Rayleigh distillation equation for $\delta^{56}Fe(II)_{aq}$ and the corresponding $\delta^{56}Fe(III)_{ppt}$ under the assumption that the $\delta^{56}Fe$ signature of the carbonates represents the $\delta^{56}Fe_{aq}$ signature of the remaining seawater $Fe(II)_{aq}$ pool after the precipitation of $Fe(III)_{ppt}$:

$$\delta^{56}Fe(II)_{aq} = (\delta^{56}Fe(II)_{aq\text{-initial}} + 1000)f^{\alpha-1} - 1000 \tag{5.4}$$

$$\delta^{56}Fe(II)_{ppt} = (\delta^{56}Fe(II)_{aq\text{-initial}} + 1000) \times \left(\frac{1 - f^{\alpha}}{1 - f}\right) - 1000 \tag{5.5}$$

with $f = \frac{Fe(II)aq}{Fe(II)aq,initial}$.

An initial $\delta^{56}Fe$ signature of seawater $Fe(II)_{aq\text{-initial}}$ of 0 permil was chosen to reflect hydrothermally derived Fe(II), which was probably the dominant contributor of $Fe(II)_{aq}$ into the anoxic open ocean, and assuming that higher hydrothermal activity in the Archean decreased fractionation effects along those systems (Jacobsen and Pimentelklose, 1988; Derry and Jacobsen, 1990; Bau and Moller, 1993; Beard and others, 2003b).

TABLE 5

Rayleigh fit of 'Shelf' and 'Slope' trendlines (fig. 8) based on $Fe(II)_{aq}$ incorporation into calcite

Location	Formation	Sample	Fe (wt-%)	Ca (wt-%)	$\frac{Fe^{2+}}{Ca^{2+}}_{calcite}$	$\frac{a_{Fe^{2+}}}{a_{Ca^{2+}}}_{solution}$	$Fe(II)_{aq}$ (mM)	$\delta^{56}Fe$ (‰)
	SHELF TRENDLINE							
	Precipitation rate: 309 µmol/h/m^2 (100 m/Ma, Altermann and Nelson, 1998); Ca^{2+}_{aq} = 20 mM; 25 °C							
	$\Sigma\chi^2$ = 1.579; $\varepsilon Fe(III)_{ppt}$-$Fe(II)_{aq}$ = 0.762 ‰; $Fe(II)_{aq\text{-}initial}$: 194 µM							
Kuruman Kop (GWA)	Gamohaan	Ku12_06	0.32	**38.36**	0.006	0.002	0.031	-1.744
		Ku12_25	1.21	35.74	0.024	0.006	0.125	-0.289
BH-1 (GWA)	Gamohaan	340	0.44	**35.89**	0.008	0.002	0.046	-1.819
		375	0.85	35.74	0.017	0.004	0.098	-0.854
BH-1 (GWA)	Reivilo	2098	0.95	35.74	0.019	0.005	0.099	-0.225
		2250	0.28	35.74	0.006	0.001	0.029	-1.065
		2275	0.29	35.74	0.006	0.002	0.030	-1.037
		2293	0.35	35.74	0.007	0.002	0.036	-1.080
		2355	0.78	35.74	0.016	0.004	0.082	-1.204
		2379	0.47	35.74	0.009	0.002	0.049	-1.068
		2400	0.34	35.74	0.007	0.002	0.035	-1.235
KMF-5 (TA)	Oaktree	1731.1	0.69	35.74	0.014	0.004	0.072	-0.668
		1731.3	0.73	35.74	0.015	0.004	0.076	-0.616
		1742.3	0.80	35.74	0.016	0.004	0.084	-0.718
		1790.1	1.29	35.74	0.026	0.007	0.135	0.083
		1800.1	1.04	35.74	0.021	0.005	0.109	-0.318
	SLOPE TRENDLINE							
	Precipitation rate: 31 µmol/h/m^2 (10 m/Ma, Altermann and Nelson, 1998); Ca^{2+}_{aq} = 20 mM; 25 °C							
	$\Sigma\chi^2$ = 5.44; $\varepsilon Fe(III)_{ppt}$-$Fe(II)_{aq}$ = 0.57 ‰; $Fe(II)_{aq\text{-}initial}$: 555 µM							
GKP01 (GWA)	upper Nauga	346.9	2.77	35.74	0.056	0.010	0.200	-0.564
		460.3	0.57	35.74	0.012	0.002	0.041	-1.055
		480.64	2.49	35.74	0.050	0.009	0.180	-0.682
		567.4	0.86	35.74	0.017	0.003	0.062	-0.264
		619	0.53	35.74	0.011	0.002	0.039	-0.843
		634.45	0.64	35.74	0.013	0.002	0.047	-0.761
		667	0.52	35.74	0.010	0.002	0.038	-1.227
	lower Nauga	693.84	0.58	35.74	0.012	0.002	0.042	-1.122
		755.51	0.57	35.74	0.011	0.002	0.041	-1.371
		796.22	0.90	35.74	0.018	0.003	0.065	-1.376
		859.9	0.91	35.74	0.018	0.003	0.066	-1.483
		911.8	0.83	35.74	0.017	0.003	0.060	-1.042
	Monteville	987.24	1.46	35.74	0.029	0.005	0.105	-1.459
GKF01 (GWA)	upper Nauga	395.4	1.36	35.74	0.027	0.005	0.098	-1.255
		570.16	0.56	35.74	0.011	0.002	0.040	-1.619
		790.18	0.41	35.74	0.008	0.001	0.030	-1.464
	lower Nauga	925.9	0.46	35.74	0.009	0.002	0.034	-2.118
		1094.84	2.09	35.74	0.042	0.008	0.152	-1.006
	Monteville	1386.26	1.45	**36.40**	0.029	0.005	0.103	-1.501
		1429.08	0.09	**34.43**	0.002	0.000	0.006	-3.685
	Lokammona	1458.42	1.63	**32.23**	0.036	0.007	0.131	-1.156
	SLOPE TRENDLINE - LIMESTONES							
	Precipitation rate: 31 µmol/h/m^2 (10 m/Ma, Altermann and Nelson, 1998); Ca^{2+}_{aq} = 20 mM; 25 °C							
	$\Sigma\chi^2$ = 0.011; $\varepsilon Fe(III)_{ppt}$-$Fe(II)_{aq}$ = 0.82 ‰; $Fe(II)_{aq\text{-}initial}$: 573 µM							
GKF01 (GWA)	Monteville	1386.26	1.45	**36.40**	0.029	0.005	0.103	-1.501
		1429.08	0.09	**34.43**	0.002	0.000	0.006	-3.685
	Lokammona	1458.42	1.63	**32.23**	0.036	0.007	0.131	-1.156

Ca concentration in bold are from XRF analyses and represent limestones. All other Ca concentrations represent an artificial calcite composition of the analyzed dolomite. All Fe concentrations and isotope signatures are from ICP-MS analyses.

TABLE 6

Calculated $Fe(II)_{aq}$-initial concentrations on different temperatures, $Ca^{2+}{}_{aq}$ concentrations and sedimentation rates

$Ca^{2+}{}_{aq}$ = 10 mM	SLOPE			SHELF		
Sedimentation rate	2 m/Ma	10 m/Ma	20 m/Ma	50 m/Ma	100 m/Ma	150 m/Ma
Temperature	$Fe(II)_{aq\text{-}initial}$ (μM)					
10°C	334	415	456	120	131	139
25°C	215	277	309	87	97	103
50°C	61	87	102	30	35	39
$Ca^{2+}{}_{aq}$ = 20 mM	SLOPE			SHELF		
Sedimentation rate	2 m/Ma	10 m/Ma	20 m/Ma	50 m/Ma	100 m/Ma	150 m/Ma
Temperature	$Fe(II)_{aq\text{-}initial}$ (μM)					
10°C	668	831	912	239	262	277
25°C	430	555	619	173	194	206
50°C	122	174	203	60	70	77
$Ca^{2+}{}_{aq}$ = 30 mM	SLOPE			SHELF		
Sedimentation rate	2 m/Ma	10 m/Ma	20 m/Ma	50 m/Ma	100 m/Ma	150 m/Ma
Temperature	$Fe(II)_{aq\text{-}initial}$ (μM)					
10°C	1003	1246	1368	358	393	416
25°C	645	832	928	260	290	310
50°C	182	261	305	96	106	116

Regression equations for Fe(II) incorporation into calcite, based on the distribution coefficient $D_{Fe^{2+}}$ for an activity ratio $\frac{a_{Fe^{2+}}}{a_{Ca^{2+}}} = 0.001$ *at* $10°C$: $\log D_{Fe(II)} = 0.79 - 0.135 \times \log (rate)$; $25°C$: $\log D_{Fe^{2+}} = 0.98 - 0.158 \times \log (rate)$; $50°C$: $\log D_{Fe^{2+}} = 1.58 - 0.223 \times \log (rate)$; (Dromgoole and Walter, 1990) (rate = precipitation (sedimentation) rate in $\mu mol/h/m^2$).

The results of these calculations are summarized in table 6 and illustrated in figure 8. The Rayleigh fit of the 'Shelf' trend results in a $Fe(II)_{aq\text{-}initial}$ of 193 μM and an $\varepsilon^{56}Fe(III)_{ppt}$-$Fe(II)_{aq}$ of +0.762 permil, with a $\Sigma\chi^2$ of −0.922. The Rayleigh fit of the 'Slope' trend yields a $Fe(II)_{aq\text{-}initial}$ of 555 μM and an $\varepsilon^{56}Fe(III)_{ppt}$-$Fe(II)_{aq}$ of +0.573 permil, however the $\Sigma\chi^2$ of 5.437 is very poor. A Rayleigh fit of the 'Slope-Limestone' (only calcitic slope carbonates) [GKF01: 1386.26, 1458.42, and 1429.08 (Czaja and others, 2012)] yields a similar $Fe(II)_{aq\text{-}initial}$ of 573 μM and a higher $\varepsilon^{56}Fe(III)_{ppt}$-$Fe(II)_{aq}$ of +0.821 permil, with a $\Sigma\chi^2$ of 0.011. However, those samples were deposited at the lowermost CMCP and there is the possibility that they do not represent the complete slope succession. The high $\Sigma\chi^2$ value of the 'Slope' trendline indicates that secondary processes, like DIR, might have had disturbed the primary Fe isotope composition of some samples (Johnson and others, 2008b; Heimann and others, 2010; Czaja and others, 2012; Johnson and others, 2013).

Our calculations show that $Fe(II)_{aq\text{-}initial}$ decreases at higher temperatures, lower $Ca^{2+}{}_{aq}$ concentrations, and a lower sedimentation rate and increases at lower temperatures, higher $Ca^{2+}{}_{aq}$ concentrations, higher sedimentation rate (table 6). These calculations suggest that $Fe(II)_{aq\text{-}initial}$ concentrations along the slope were between 61 μM (50 °C, 10 mM $Ca^{2+}{}_{aq}$, 2 m/Ma sedimentation rate) and 1368 μM (10 °C, 30 mM $Ca^{2+}{}_{aq}$, 20 m/Ma sedimentation rate), whereas $Fe(II)_{aq\text{-}initial}$ concentrations in the shallow marine environment of the shelf were between 30 μM (50 °C, 10 mM $Ca^{2+}{}_{aq}$, 50 m/Ma sedimentation rate) and 394 μM (10 °C, 30 mM $Ca^{2+}{}_{aq}$, 150 m/Ma sedimentation rate). This is a huge span and emphasizes the strong dependency of

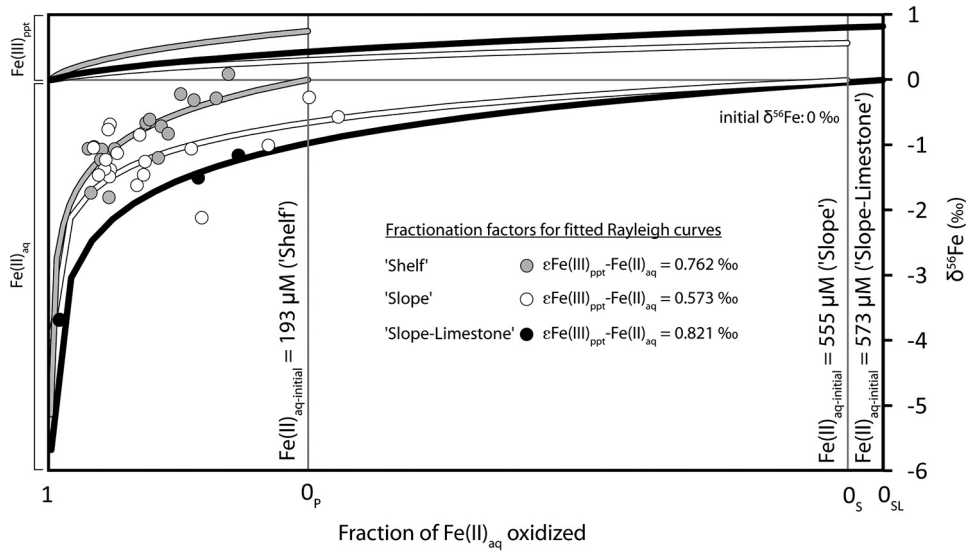

Fig. 8. Rayleigh fits of curves for 'Shelf' and 'Slope' trendlines (figs. 4 C-4D), based on the calculations in table 5. 'Slope-Limestone' curve is fitted for calcitic carbonate samples from the slope succession (GKF01). Curves have different initial $Fe(II)_{aq}$ concentration. 0_P, 0_S, and 0_{SL} anchor 'Shelf', 'Slope', and 'Slope Limestone' trendlines, respectively.

dissolved $Fe(II)_{aq}$ in seawater on external factors. Early estimates of seawater temperatures for the Archean of ~70 to 85 °C (Karhu and Epstein, 1986; Knauth and Lowe, 2003), based on oxygen isotope data of cherts, have been criticized as too high and recent estimates argue for a maximum of 26 °C (de Wit and Furnes, 2016) to 40 °C (Hren and others, 2009). Blake and others (2010) also proposed a range between 26 and 35 °C, based on oxygen isotopes in phosphates. Assuming that seawater temperatures were around 25°, this limits the range of $Fe(II)_{aq}$ concentrations in this simulation between 215 and 928 µM for the open marine slope and 87 to 310 µM for the shallow-marine shelf succession for varying Ca^{2+}_{aq} (Horiata and others, 2002; Canfield, 2005) and sedimentation rates (Altermann and Nelson, 1998). This is still a large range but regardless of the exact conditions prevailing in seawater, there are two important implications. First, $Fe(II)_{aq}$ concentrations in seawater were probably higher than the previously assumed 3 to 360 µM for the open ocean (Holland, 1973; Morris, 1993; Canfield, 2005) and 10 µM for shallow seawater (Riding and others, 2014). Secondly, a concentration gradient existed, with higher $Fe(II)_{aq}$ concentrations along the deeper slope facies and lower $Fe(II)_{aq}$ concentrations in the shallow shelf facies. This implies the removal of $Fe(II)_{aq}$ supplied during upwelling along the carbonate platform margin, probably due to a chemocline between ferruginous deeper water and oxygenated shallow water. This is also implied by the calculated fractionation of the Rayleigh fits ($\varepsilon^{56}Fe(III)_{ppt}$-$Fe(II)_{aq}$ of +0.573 ‰ or +0.821 ‰ for the 'Slope' trend and +0.762 ‰ for the 'Shelf' trend), even though those are slightly lower than the reported fractionation of 1 to 3 permil, during oxidation by dissolved oxygen or by microbially-induced oxidation (Bullen and others, 2001; Beard and others, 2003a; Croal and others, 2004; Balci and others, 2006; Kappler and others, 2010; Swanner and others, 2015b). This diminished fractionation factor is likely due to transport effects and the range of ages and reaction extent for Fe-bearing waters from which the carbonates formed (Druhan and Maher, 2017). Lower $Fe(II)_{aq}$ concentrations on the shelf would also lower the risk of Fe toxicity for cyanobacteria and increase their ability

to produce oxygen (Swanner and others, 2015a). This reinforces the assumption of a change from an anaerobic to an aerobic ecosystem in the CMCP.

Implications for the Neoarchean Shallow Marine Environment and for Carbonates as Fe Redox Proxies

Carbonate platforms and their shallow-marine environment were probably the first site of oxygenic photosynthesis and are the interface of marine and terrestrial processes. Thus, they are valuable archives of the Neoarchean marine Fe cycle, when oceans likely had dissolved Fe concentrations of tens to hundreds of μM than today's ocean with only a few nM of dissolved Fe. The main sources of Fe into the Archean ocean were from hydrothermal vents and the continents, which likely remobilized along continental margins during microbially driven reduction processes in the sediment (Severmann and others, 2008; Li and others, 2015). Marine Ca-Mg carbonates that incorporate $Fe(II)_{aq}$ directly from seawater could even reflect the Fe seawater signal, although sedimentary redox processes can affect primary signatures. Fe concentration, isotope composition and speciation in Ca-Mg carbonates and mudrocks of the Neoarchean CMCP can thus give valuable insights into the dynamics of the continental and hydrothermal Fe sources and unravel redox processes influencing the Fe inventory in shallow-marine systems, where oxygen was likely produced by photosynthesis. Figure 9 shows the reconstructed Fe sources and cycles based on the different stages of the CMCP. During the initial flooding of the Kaapvaal Craton ~2.6 Ga ago (fig. 9, stage 1), carbonates mainly exchanged with open ocean water, and Fe isotope signatures and concentrations indicate Rayleigh distillation of Fe by aerobe or anaerobe oxidation. Data also indicate a concentration gradient with higher $Fe(II)_{aq}$ concentrations in the slope facies than in the platform facies. This is supported by REE+Y data, showing a shift from hydrothermal dominated signatures to signatures typical for Archean shallow seawater (fig. S2b, supplementary material, http://earth.geology.yale.edu/%7eajs/SupplementaryData/2018/Eroglu). Fe(II)-minerals in carbonates indicate sedimentary redox conditions below Fe reduction. With continuing growth of the platform a steep ramp architecture developed (fig. 9, stage 2), which was still connected to the ocean, however during events of regression, influx of continental material and freshwater were of greater importance. This is shown by the frequent occurrence of organic-rich mudrocks in the peritidal succession of the platform and the change in REE+Y patterns that record an increasing influence of the continent (fig. S2b, supplementary material). Even though the influx of ocean water was probably diminished, maybe allowing a shift to a more aerobic ecosystem, the overall conditions in the sediment were still dominantly reducing, as carbonates and mudrocks solely contain Fe(II)-minerals. Overall, the lower CMCP was dominated by secondary remobilization of Fe via microbially-driven diagenesis, leading to a shelf-to basin Fe shuttle, where incomplete reduction of reactive Fe in shelf sediments releases isotopically light $Fe(II)_{aq}$, which is transported to the slope, leaving the residual Fe in the shelf isotopically heavy. The deposition of the Kamden Member iron formation was a short intense transgressive event and is reflected in very Fe-rich sediments, even in the very shallow-marine platform succession (fig. 9, stage 3). There, the intense influx of open ocean water is implicated by a clear positive Eu anomaly in a siliciclastic-rich carbonate (fig. S2b, supplementary material). During this major transgression, the provided accommodation space was rapidly filled and rimmed margin architecture developed (fig. 9, stage 4), which drastically changed the environmental conditions in the upper CMCP. Due to the special rimmed margin the influx of open ocean water was very poor and a restricted lagoon in the platform interior could develop. Due to the reduced influx of hydrothermal species, the ecosystem probably changed and aerobe microorganisms dominated the lagoonal interior (Eroglu and others, 2017). The relatively enhanced influx of freshwater, indicated by flattened REE+Y patterns (fig. S2b,

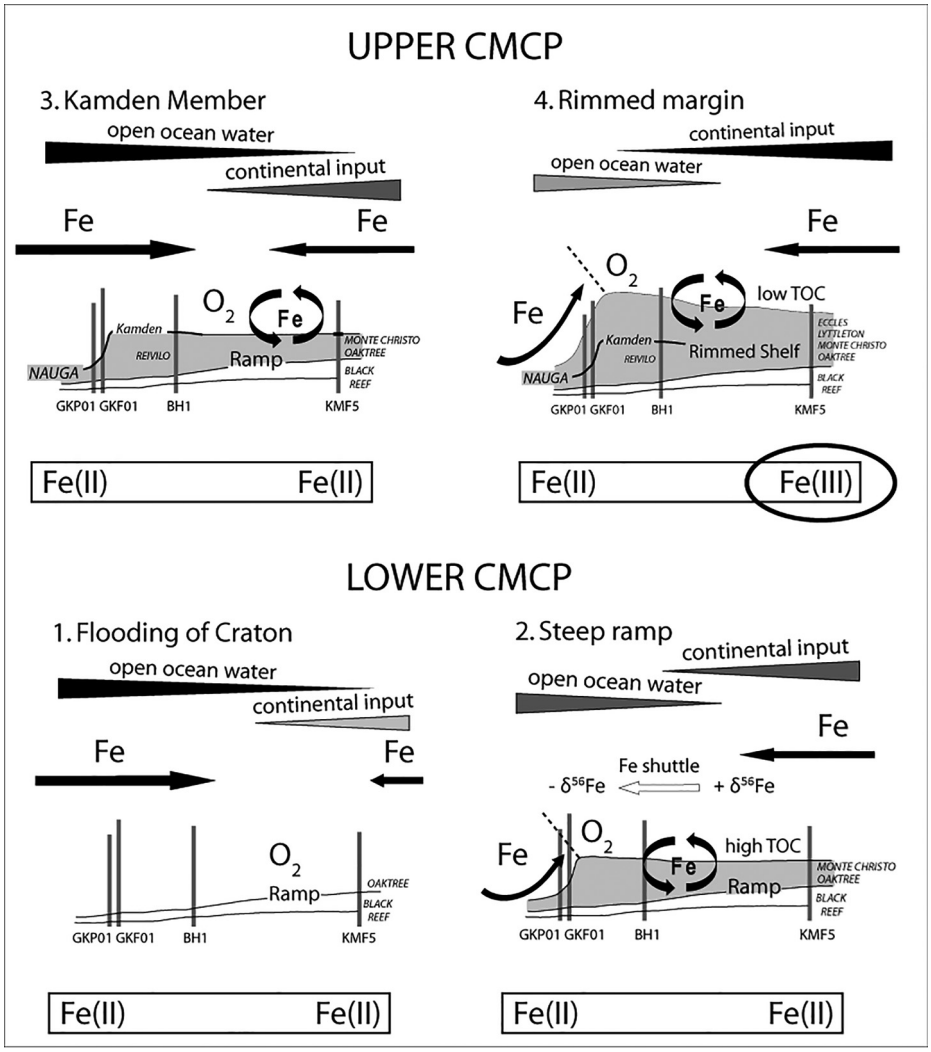

Fig. 9. Fe sources and cycles reflect paleoenvironmental conditions of the CMCP over time (modified after Eroglu and others, 2017).

supplementary material), fueled silicification in the peritidal facies, as it was still mainly exposed to the open ocean, which is indicated by REE+Y signatures that show higher REE+Y concentrations and a more pronounced Eu anomaly. Interestingly, carbonates of the restricted platform interior are dominated by Fe(III)-minerals that also implicate an increase in the oxidation state of the platform. Fe systematics are still mainly controlled by secondary sedimentary processes, although the scarcity of organic-rich mudrocks probably changed the intensity of reductive Fe mobilization in the sediment.

Carbonates deposited during open marine conditions record a Rayleigh distillation of ferruginous deeper water by reaction with oxygenated shallow water, although an oxidation by anoxygenic photosynthesis cannot be ruled out. Calculations of $Fe(II)_{aq}$ incorporation into calcite indeed imply a concentration gradient from the slope facies to the shelf facies of the CMCP and support the loss of $Fe(II)_{aq}$ via

oxidation and precipitation of $Fe(III)_{ppt}$. Those findings support the existence of an oxic-anoxic boundary probably in several hundred meters water depth (Kendall and others, 2010) of the Neoarchean ocean, although an anoxygenic photosynthetic Fe(II) oxidation pathway cannot be ruled out. Following this, $Fe(II)_{aq}$ concentration estimates range from 61 to 928 μM $Fe(II)_{aq}$ for the slope and 30 to 310 μM $Fe(II)_{aq}$ for the shelf setting, depending on assumed seawater temperature, Ca^{2+} concentration in seawater and sedimentation rate.

Carbonates deposited in the peritidal settings and during the rimmed margin stage reveal that Fe cycling in the shelf interior was dominated by freshwater input from the continent and early diagenetic Fe remobilization in the soft sediment, in particular from adjacent mudrocks. Hereby, Fe would have been rather added from leaching and dissolution of siliciclastics, sulfides and oxyhydroxides to altered carbonates (Veizer, 1983). There is no indication that dolomitization and silicification affected the Fe isotope signatures. Based on these observations, it is likely that Fe was already incorporated during the initial carbonate precipitation and did not change significantly during dolomitization.

Fe speciation of CMCP carbonates reveal an increase in oxidation state throughout the platform, with a Fe(II)-dominated speciation in the lower CMCP and a Fe(III)-dominated speciation in the upper CMCP. This can be explained by a lower content of reductants in the upper CMCP, in particular organic carbon and sulfide species, and by the rimmed margin architecture, protecting the shelf environment from reducing species from the anoxic open ocean.

Following from the observed dependence of the Fe concentration on water depth (fig. 4D), $Fe(II)_{aq}$ was most likely mainly delivered from seawater and interacted with the sediment surface, where it could have been directly incorporated into the calcite structure (Dromgoole and Walter, 1990; Mettler, ms, 2002). Thus, for the Ca-Mg carbonates, which were exposed to the open ocean, it can be suggested that the Fe incorporated into the dolomite structure rather stemmed from the recrystallized calcite itself and not from an external (continental) source. In contrast, detrital and riverine input of Fe into the peritidal environment clearly affected the local carbonates (fig. 4C) and can explain variable Fe concentrations of carbonate in those restricted settings. All these observations agree with the major and trace element results and show that the Fe budget was controlled by the depositional environment and the relative input from the open ocean and the continent. This affirms the quality of dolomitized carbonate as a proxy for Fe in ancient marine environments and allows implications to be drawn on the redox processes in coeval seawater and sediment.

CONCLUSIONS

In this study, we present new Fe isotope and concentration data of Ca-Mg carbonates and mudstones from the shelf setting of the CMCP. In combination with an earlier study about the slope setting of the CMCP (Czaja and others, 2012), we were able to interpret the Fe systematics of several spatial and temporal depositional settings of the CMCP. We show that the Fe systematics are highly dependent on the water source, that is open ocean vs. freshwater, and that the platform architecture is an important factor delineating water sources. Carbonate sections that were deposited during extensive interaction with open ocean water, for instance along the slope and during transgression events, record an Fe pool that is diminishing in concentration and becoming isotopically lighter with decreasing water depth, consistent with being the residual $Fe(II)_{aq}$ remaining after Fe oxidation.

$Fe(II)_{aq}$ concentrations in seawater were probably about two to three times higher along the slope than on the shelf due to higher exchange with open ocean water. Estimates of $Fe(II)_{aq}$ at conditions of 25 °C water temperature, a $Ca^{2+}{}_{aq}$ concentration of 20 mM, and a sedimentation rate of 100 m/Ma along the shelf and 10 m/Ma along

the slope, are 193 μM for shallow-marine seawater and 555 μM for the open ocean. These estimations are higher than earlier estimates, and are strongly dependent on assumed water temperature, sedimentation rate and $Ca^{2+}{}_{aq}$ concentration in the seawater. Our findings agree with other studies that propose a decrease in Fe concentration with decreasing water depth, likely due to the removal of Fe along an oxic-anoxic chemocline (for example Beukes, 1987; Sumner and Grotzinger, 1996; Beukes and Gutzmer, 2008; Riding and others, 2014).

Fe systematics in carbonate successions, deposited during peritidal conditions with restricted access of open ocean water and contain abundant mudrock layers, rather reflect early diagenetic Fe remobilization, driven by degradation of organic matter. Localized diagenetic element cycling is also supported by secondary Fe-sulfides present in mudrocks and some carbonates. Heavy δ^{56}Fe signatures in mudrocks of the shelf succession compared to light δ^{56}Fe in mudrocks from the slope succession indicate a shelf-to-basin Fe shuttle, where incomplete reduction of reactive Fe in shelf sediments releases isotopically light $Fe(II)_{aq}$, which is transported to and recycled in the slope sediment, leaving the residual Fe in the shelf sediment isotopically heavy. Those early diagenetic processes also affected adjacent carbonates and their Fe inventory and isotope signature due to circulating pore fluids.

Fe speciation changes over time in the carbonates of the CMCP. In the lower CMCP Fe(II) phases dominate, incorporated into the dolomite structure and as distinctive Fe(II)-sulfides in the sediment. This changes towards the upper CMCP, as soon as the rimmed margin was formed, when Fe(III)-(oxyhydr)oxides dominate the shallow-marine shelf facies and are incorporated in Ca-Mg carbonate.

We propose that Fe isotope signatures and concentrations of Ca-Mg carbonates can serve as good proxies for paleoenvironmental reconstructions and biogeochemical processes of ancient shallow marine settings. Thereby, it is crucial to complement the isotope data with other mineralogical, sedimentological, and geochemical information of the targeted carbonate setting to evaluate diagenetic alteration of the primary isotopic signals. For future studies other ancient and modern carbonate platforms are interesting targets, in order to see if there is a similar systematic like in the CMCP. Furthermore, detailed studies on the behavior of Fe in microbial mats and stromatolitic carbonates are necessary to provide a framework for more precise interpretation of the processes affecting Fe concentrations and their isotopic composition in carbonates.

ACKNOWLEDGMENT

Financial support for this project was provided by the German Research Council (DFG) grant SCHO1071/4 to RS, of a postdoctoral fellowship from the Carl-Zeiss Foundation and the '*Nachwuchswissenschaftlerinnen*' funding of the University of Tübingen to EDS, and of the Fulbright Commission to SE. The XANES measurements were performed on beamline ID24 at the European Synchrotron Radiation Facility (ESRF), Grenoble, France. We are grateful to S. Pascarelli at the ESRF for providing assistance in using beamline ID24. We thank the reviewers S. Lalonde, J. Marin-Carbonne, and L. Robbins for their helpful and constructing comments. We also thank Associate Editor N. Planavsky. F. Hasiuk, F. Kurzweil, A. Mucci, M. Wille, and W. Wu are thanked for valuable discussions. F. Perrin is thanked for support during synchrotron measurements. A. Sole and A. Picard are thanked for support during evaluation of the XANES data. I. Gill-Kopp, P. Jeisecke, and S. Schafflick prepared rock thin sections at the University of Tübingen. Scott Schlorholtz conducted XRD analyses at the Material Analyses and Research Lab (MARL) at the Iowa State University.

REFERENCES

Altermann, W., and Nelson, D. R., 1998, Sedimentation rates, basin analysis and regional correlations of three Neoarchaean and Palaeoproterozoic sub-basins of the Kaapvaal craton as inferred from precise U-Pb zircon ages from volcaniclastic sediments: Sedimentary Geology, v. 120, n. 1–4, p. 225–256, https://doi.org/10.1016/S0037-0738(98)00034-7

Altermann, W., and Siegfried, H. P., 1997, Sedimentology and facies development of an Archaean shelf: Carbonate platform transition in the Kaapvaal Craton, as deduced from a deep borehole at Kathu, South Africa: Journal of African Earth Sciences, v. 24, n. 3, p. 391–410, https://doi.org/10.1016/S0899-5362(97)00051-1

Anbar, A. D., Duan, Y., Lyons, T. W., Arnold, G. L., Kendall, B., Creaser, R. A., Kaufman, A. J., Gordon, G. W., Scott, C., Garvin, J., and Buick, R., 2007, A whiff of oxygen before the Great Oxidation Event?: Science, v. 317, n. 5846, p. 1903–1906, https://doi.org/10.1126/science.1140325

Balci, N., Bullen, T. D., Witte-Lien, K., Shanks, W. C., Motelica, M., and Mandernack, K. W., 2006, Iron isotope fractionation during microbially stimulated Fe(II) oxidation and Fe(III) precipitation: Geochimica et Cosmochimica Acta, v. 70, n. 3, p. 622–639, https://doi.org/10.1016/j.gca.2005.09.025

Banner, J. L., 1995, Application of the Trace-Element and Isotope Geochemistry of Strontium to Studies of Carbonate Diagenesis: Sedimentology, v. 42, n. 5, p. 805–824, https://doi.org/10.1111/j.1365-3091.1995.tb00410.x

Bau, M., and Möller, P., 1993, Rare-Earth Element Systematics of the Chemically Precipitated Component in Early Precambrian Iron Formations and the Evolution of the Terrestrial Atmosphere-Hydrosphere-Lithosphere System: Geochimica et Cosmochimica Acta, v. 57, n. 10, p. 2239–2249, https://doi.org/10.1016/0016-7037(93)90566-F

Beard, B. L., Johnson, C. M., Skulan, J. L., Nealson, K. H., Cox, L., and Sun, H., 2003a, Application of Fe isotopes to tracing the geochemical and biological cycling of Fe: Chemical Geology, v. 195, n. 1–4, p. 87–117, https://doi.org/10.1016/S0009-2541(02)00390-X

Beard, B. L., Johnson, C. M., Von Damm, K. L., and Poulson, R. L., 2003b, Iron isotope constraints on Fe cycling and mass balance in oxygenated Earth oceans: Geology, v. 31, n. 7, p. 629–632, https://doi.org/10.1130/0091-7613(2003)031<0629:IICOFC>2.0.CO;2

Beard, B. L., Handler, R. M., Scherer, M. M., Wu, L. L., Czaja, A. D., Heimann, A., and Johnson, C. M., 2010, Iron isotope fractionation between aqueous ferrous iron and goethite: Earth and Planetary Science Letters, v. 295, n. 1–2, p. 241–250, https://doi.org/10.1016/j.epsl.2010.04.006

Bekker, A., Slack, J. F., Planavsky, N., Krapez, B., Hofmann, A., Konhauser, K. O., and Rouxel, O. J., 2010, Iron Formation: The Sedimentary Product of a Complex Interplay among Mantle, Tectonic, Oceanic, and Biospheric Processes: Economic Geology, v. 105, n. 3, p. 467–508, https://doi.org/10.2113/gsecongeo.105.3.467

Bergquist, B. A., and Boyle, E. A., 2006, Iron isotopes in the Amazon River system: Weathering and transport signatures: Earth and Planetary Science Letters, v. 248, n. 1–2, p. 54–68, https://doi.org/10.1016/j.epsl.2006.05.004

Berner, R. A., 1981, A New Geochemical Classification of Sedimentary Environments: Journal of Sedimentary Petrology, v. 51, n. 2, p. 359–365, https://doi.org/10.1306/212F7C7F-2B24-11D7-8648000102C1865D

Beukes, N. J., 1987, Facies Relations, Depositional-Environments and Diagenesis in a Major Early Proterozoic Stromatolitic Carbonate Platform to Basinal Sequence, Campbellrand Subgroup, Transvaal Supergroup, Southern-Africa: Sedimentary Geology, v. 54, n. 1–2, p. 1–46, https://doi.org/10.1016/0037-0738(87)90002-9

Beukes, N. J., and Gutzmer, J., 2008, Origin and paleoenvironmental significance of major iron formations at the Archean-Paleoproterozoic Boundary, *in* Hageman, S., Rosiere, C., Gutzmer, J., and Beukes, N., editors, Banded Iron Formation-Related High Grade Ore: Society of Economic Geologists, Reviews in Economic Geology, v. 15, 5–47, https://doi.org/10.5382/Rev.15.01

Blake, R. E., Chang, S. J., and Lepland, A., 2010 Phosphate oxygen isotopic evidence for a temperate and biologically active Archaean ocean: Nature. v. 464, p. 1029–1032, https://doi.org/10.1038/nature08952

Brand, U., and Veizer, J., 1980, Chemical Diagenesis of a Multicomponent Carbonate System .1. Trace-Elements: Journal of Sedimentary Petrology, v. 50, n. 4, p. 1219–1236, https://doi.org/10.1306/212F7BB7-2B24-11D7-8648000102C1865D

Brucker, R. L. P., McManus, J., Severmann, S., and Berelson, W. M., 2009, Molybdenum behavior during early diagenesis: Insights from Mo isotopes: Geochemistry, Geophyics, Geosystems, v. 10, n. 6, https://doi.org/10.1029/2008GC002180

Bullen, T. D., White, A. F., Childs, C. W., Vivit, D. V., and Schulz, M. S., 2001, Demonstration of significant abiotic iron isotope fractionation in nature: Geology, v. 29, n. 8, p. 699–702, https://doi.org/10.1130/0091-7613(2001)029<0699:DOSAII>2.0.CO;2

Busigny, V., Planavsky, N. J., Jézéquel, D., Crowe, S., Louvat, P., Moureau, J., Viollier, E., and Lyons, T. W., 2014, Iron isotopes in an Archean ocean analogue: Geochimica et Cosmochimica Acta, v. 133, p. 443–462, https://doi.org/10.1016/j.gca.2014.03.004

Butler, I. B., Archer, C., Vance, D., Oldroyd, A., and Rickard, D., 2005, Fe isotope fractionation on FeS formation in ambient aqueous solution: Earth and Planetary Science Letters, v. 236, n. 1–2, p. 430–442, https://doi.org/10.1016/j.epsl.2005.05.022

Button, A., 1973, The stratigraphic history of the Malmani Dolomite in the eastern and north-eastern Transvaal: Transactions of the Geological Society of South Africa, v. 76, p. 229–247.

Canfield, D. E., 2005, The early history of atmospheric oxygen: Homage to Robert A. Garrels: Annual Review of Earth and Planetary Sciences, v. 33, p. 1–36, https://doi.org/10.1146/annurev.earth.33.092203.122711

Chai, L., and Navrotsky, A., 1996, Synthesis, characterization, and energetics of solid solution along the dolomite-ankerite join, and implications for the stability of ordered $CaFe(CO_3)_2$: American Mineralogist, v. 81, 9–10, p. 1141–1147, https://doi.org/10.2138/am-1996-9-1012

Cloud, P. E, Jr., 1968, Atmospheric and Hydrospheric Evolution on Primitive Earth: Science, v. 160, p. 729–736, https://doi.org/10.1126/science.160.3829.729

Coetzee, L. L., ms, 2001, Genetic stratigraphy of the Paleoproterozoic Pretoria Group in the western Transvaal: Johannesburg, South Africa, Rand Afrikaans University, M. Sc. thesis, p. 184.

Cornell, R. M., and Schwertmann, U., 2003, The Iron Oxides: Structure, Properties, Reactions, Occurrences and Uses: Weinhem, Germany, Wiley-VCH Verlag GmbH, 664 p. https://doi.org/10.1002/3527602097

Craddock, P. R., and Dauphas, N., 2011, Iron and carbon isotope evidence for microbial iron respiration throughout the Archean: Earth and Planetary Science Letters, v. 303, n. 1–2, p. 121–132, https://doi.org/10.1016/j.epsl.2010.12.045

Craddock, P. R., Warren, J. M., and Dauphas, N., 2013, Abyssal peridotites reveal the near-chondritic Fe isotopic composition of the Earth: Earth and Planetary Science Letters, v. 365, p. 63–76, https://doi.org/10.1016/j.epsl.2013.01.011

Croal, L. R., Johnson, C. M., Beard, B. L., and Newman, D. K., 2004, Iron isotope fractionation by Fe(II)-oxidizing photoautotrophic bacteria: Geochimica et Cosmochimica Acta, v. 68, n. 8, p. 1227–1242, https://doi.org/10.1016/j.gca.2003.09.011

Crowe, S. A., Jones, C., Katsev, S., Magen, C., O'Neill, A. H., Sturm, A., Canfield, D. E., Haffner, G. D., Mucci, A., Sundby, B., and Fowle, D. A., 2008, Photoferrotrophs thrive in an Archean Ocean analogue: Proceedings of the National Academy of Sciences of the United States of America, v. 105, n. 41, p. 15938–15943, https://doi.org/10.1073/pnas.0805313105

Crowe, S. A., Dossing, L. N., Beukes, N. J., Bau, M., Kruger, S. J., Frei, R., and Canfield, D. E., 2013, Atmospheric oxygenation three billion years ago: Nature, v. 501, p. 535–38, https://doi.org/10.1038/nature12426

Czaja, A. D., Johnson, C. M., Roden, E. E., Beard, B. L., Voegelin, A. R., Nagler, T. F., Beukes, N. J., and Wille, M., 2012, Evidence for free oxygen in the Neoarchean ocean based on coupled iron-molybdenum isotope fractionation: Geochimica et Cosmochimica Acta, v. 86, p. 118–137, https://doi.org/10.1016/j.gca.2012.03.007

Dauphas, N., and Rouxel, O., 2006, Mass spectrometry and natural variations of iron isotopes: Mass Spectrometry Reviews, v. 25, n. 4, p. 515–550, https://doi.org/10.1002/mas.20078

de Baar, H. J. W., and de Jong, J. T. M., 2001, Distributions, sources and sinks of iron in seawater, *in* Turner, D. R., and Hunter, K. A., editors, The Biogeochemistry of Iron in Seawater: New York, John Wiley & Sons, IUPAC Book Series on Analytical and Physical Chemistry of Environmental Systems, v. 7, p. 123–253.

de Kock, M. O., Evans, D. A. D., Kirschvink, J. L., Beukes, N. J., Rose, E., and Hilburn, I., 2009, Paleomagnetism of a Neoarchean-Paleoproterozoic carbonate ramp and carbonate platform succession (Transvaal Supergroup) from surface outcrop and drill core, Griqualand West region, South Africa: Precambrian Research, v. 169, n. 1–4, p. 80–99, https://doi.org/10.1016/j.precamres.2008.10.015

de Wit, M. J., and Furnes, H., 2016, 3.5-Ga hydrothermal fields and diamictites in the Barberton Greenstone Belt-Paleoarchean crust in cold environments: Science Advances, v. 2, n. 2, https://doi.org/10.1126/sciadv.1500368

Derry, L. A., and Jacobsen, S. B., 1990, The Chemical Evolution of Precambrian Seawater: Evidence from Rees in Banded Iron Formations: Geochimica et Cosmochimica Acta, v. 54, n. 11, p. 2965–2977, https://doi.org/10.1016/0016-7037(90)90114-Z

Des Marais, D. J., 2001, Isotopic evolution of the biogeochemical carbon cycle during the Precambrian, *in* Valley, J. W., and Cole, D. R., editors, Stable Isotope Geochemistry: Reviews in Mineralogy and Geochemistry, v. 43, n. 1, p. 555–578, https://doi.org/10.2138/gsrmg.43.1.555

Dideriksen, K., Baker, J. A., and Stipp, S. L. S., 2006, Iron isotopes in natural carbonate minerals determined by MC-ICP-MS with a ^{58}Fe-^{54}Fe double spike: Geochimica et Cosmochimica Acta, v. 70, n. 1, p. 118–132, https://doi.org/10.1016/j.gca.2005.08.019

Dromgoole, E. L., and Walter, L. M., 1990, Iron and Manganese Incorporation into Calcite: Effects of Growth-Kinetics, Temperature and Solution Chemistry: Chemical Geology, v. 81, n. 4, p. 311–336, https://doi.org/10.1016/0009-2541(90)90053-A

Druhan, J. L., and Maher, K., 2017, The influence of mixing on stable isotope ratios in porous media: A revised Rayleigh model: Water Resources Research, v. 53, n. 2, p. 1101–1124, https://doi.org/10.1002/2016WR019666

Eriksson, K. A., 1977, Tidal flat and subtidal sedimentation in the 2250 m.y. Malmani Dolomite, Transvaal South Africa: Sedimentary Geology, v. 18, n. 1–3, p. 223–244, https://doi.org/10.1016/0037-0738(77)90013-6

Eriksson, K. A., and Truswell, J. F., 1973, High inheritance elongate stromatolitic mounds from the Tranvaal dolomite: Paleontology of Africa, v. 1–5, n. 12, p. 23–28, http://hdl.handle.net/10539/16035

Eriksson, K. A., McCarthy, T. S., and Truswell, J. F., 1975, Limestone Formation and Dolomitization in a Lower Proterozoic Succession from South-Africa: Journal of Sedimentary Petrology, v. 45, n. 3, p. 604–614, https://doi.org/10.1306/212F6DED-2B24-11D7-8648000102C1865D

Eroglu, S., Schoenberg, R., Wille, M., Beukes, N., and Taubald, H., 2015, Geochemical stratigraphy, sedimentology, and Mo isotope systematics of the *ca.* 2.58–2.50 Ga-old Transvaal Supergroup carbonate platform, South Africa: Precambrian Research, v. 266, p. 27–46, https://doi.org/10.1016/j.precamres.2015.04.014

Eroglu, S., van Zuilen, M. A., Taubald, H., Drost, K., Wille, M., Swanner, E. D., Beukes, N. J., and Schoenberg, R., 2017, Depth-dependent $\delta^{13}C$ trends in platform and slope settings of the Campbellrand-Malmani

carbonate platform and possible implications for Early Earth oxygenation: Precambrian Research, v. 302, p. 122–139, https://doi.org/10.1016/j.precamres.2017.09.018
Fischer, W. W., Schröder, S., Lacassie, J. P., Beukes, N. J., Goldberg, T., Strauss, H., Horstmann, U. E., Schrag, D. P., and Knoll, A. H., 2009, Isotopic constraints on the Late Archean carbon cycle from the Transvaal Supergroup along the western margin of the Kaapvaal Craton, South Africa: Precambrian Research, v. 169, n. 1–4, p. 15–27, https://doi.org/10.1016/j.precamres.2008.10.010
Frauenstein, F., Veizer, J., Beukes, N., Van Niekerk, H. S., and Coetzee, L. L., 2009, Transvaal Supergroup carbonates: Implications for Paleoproterozoic δ^{18} O and δ^{13} C records: Precambrian Research, v. 175, n. 1–4, p. 149–160, https://doi.org/10.1016/j.precamres.2009.09.005
Frei, R., Gaucher, C., Poulton, S. W., and Canfield, D. E., 2009, Fluctuations in Precambrian atmospheric oxygenation recorded by chromium isotopes: Nature, v. 461, p. 250–253, https://doi.org/10.1038/nature08266
Froelich, P. N., Klinkhammer, G. P., Bender, M. L., Luedtke, N. A., Heath, G. R., Cullen, D., Dauphin, P., Hammond, D., Hartman, B., and Maynard, V., 1979, Early oxidation of organic matter in pelagic sediments of the eastern equatorial Atlantic: Suboxic diagenesis: Geochimica et Cosmochimica Acta, v. 43, n. 7, p. 1075–1090, https://doi.org/10.1016/0016-7037(79)90095-4
Garrels, R. M., and Perry, E. A., 1974, Cycling of carbon, sulfur, and oxygen through geologic time, *in* Goldberg, E. D., editor, The Sea: New York, John Wiley & Sons, p. 303–336.
Godfrey, L. V., and Falkowski, P. G., 2009, The cycling and redox state of nitrogen in the Archaean ocean: Nature Geoscience, v. 2, p. 725–729, https://doi.org/10.1038/ngeo633
Gumsley, A. P., Chamberlain, K. R., Bleeker, W., Söderlund, U., de Kock, M. O., Larsson, E. R., and Bekker, A., 2017, Timing and tempo of the Great Oxidation Event: Proceedings of the National Academy of Sciences of the United States of America, v. 114, n. 8, p. 1811–1816, https://doi.org/10.1073/pnas.1608824114
Hegler, F., Posth, N. R., Jiang, J., and Kappler, A., 2008, Physiology of phototrophic iron(II)-oxidizing bacteria: Implications for modern and ancient environments: FEMS Microbiology Ecology, v. 66, n. 2, p. 250–260, https://doi.org/10.1111/j.1574-6941.2008.00592.x
Heimann, A., Johnson, C. M., Beard, B. L., Valley, J. W., Roden, E. E., Spicuzza, M. J., and Beukes, N. J., 2010, Fe, C, and O isotope compositions of banded iron formation carbonates demonstrate a major role for dissimilatory iron reduction in ~ 2.5 Ga marine environments: Earth and Planetary Science Letters, v. 294, n. 1–2, p. 8–18, https://doi.org/10.1016/j.epsl.2010.02.015
Herzog, R. E., Shi, Q. H., Patil, J. N., and Katz, J. L., 1989, Magnetic Water-Treatment: The Effect of Iron on Calcium-Carbonate Nucleation and Growth: Langmuir, v. 5, n. 3, p. 861–867, https://doi.org/10.1021/la00087a048
Hodgskiss, M. S. W., Kunzmann, M., Poirier, A., and Halverson, G. P., 2018, The role of microbial iron reduction in the formation of Proterozoic molar tooth structures: Earth and Planetary Science Letters, v. 482, p. 1–11, https://doi.org/10.1016/j.epsl.2017.10.037
Holland, H. D., 1973, The Oceans; A Possible Source of Iron in Iron-Formations: Economic Geology, v. 68, n. 7, p. 169–1172, https://doi.org/10.2113/gsecongeo.68.7.1169
——— 1984, The Chemical Evolution of the Atmosphere and Oceans: Princeton, New Jersey, University Press, 598 p.
——— 2004, The geological history of seawater, *in* Elderfield, H., editor, The Oceans and Marine Geochemistry: Treatise on Geochemsitry, v. 6 p. 583–625, https://doi.org/10.1016/B0-08-043751-6/06122-3
Horita, J., Zimmermann, H., and Holland, H. D., 2002, Chemical evolution of seawater during the Phanerozoic: Implications from the record of marine evaporites: Geochimica et Cosmochimica Acta, v. 66, n. 21, p. 3733–3756, https://doi.org/10.1016/S0016-7037(01)00884-5
Hren, M. T., Tice, M. M., and Chamberlain, C. P., 2009, Oxygen and hydrogen isotope evidence for a temperate climate 3.42 billion years ago: Nature, v. 462, p. 205–208, https://doi.org/10.1038/nature08518
Isley, A. E., and Abbott, D. H., 1999, Plume-related mafic volcanism and the deposition of banded iron formation: Journal of Geophysical Research-Solid Earth, v. 104, n. B7, p. 15461–15477, https://doi.org/10.1029/1999JB900066
Jacobsen, S. B., and Pimentelklose, M. R., 1988, A Nd Isotopic Study of the Hamersley and Michipicoten Banded Iron Formations: The Source of Ree and Fe in Archean Oceans: Earth and Planetary Science Letters, v. 87, n. 1–2, p. 29–44, https://doi.org/10.1016/0012-821X(88)90062-3
Johnson, C., Beard, B., and Roden, E., 2008a, Temporal variations in Fe isotope compositions of banded iron formations record changes in the nature of redox cycling: Geochimica et Cosmochimica Acta, v. 72, A435–A435.
Johnson, C. M., Beard, B. L., Beukes, N. J., Klein, C., and O'Leary, J. M., 2003, Ancient geochemical cycling in the Earth as inferred from Fe isotope studies of banded iron formations from the Transvaal Craton: Contributions to Mineralogy and Petrology, v. 144, n. 5, p. 523–547, https://doi.org/10.1007/s00410-002-0418-x
Johnson, C. M., Beard, B. L., Klein, C., Beukes, N. J., and Roden, E. E., 2008b, Iron isotopes constrain biologic and abiologic processes in banded iron formation genesis: Geochimica et Cosmochimica Acta, v. 72, n. 1, p. 151–169, https://doi.org/10.1016/j.gca.2007.10.013
Johnson, C. M., Beard, B. L., and Roden, E. E., 2008c, The iron isotope fingerprints of redox and biogeochemical cycling in modern and ancient Earth: Annual Review of Earth Planetary Sciences, v. 36, p. 457–493, https://doi.org/10.1146/annurev.earth.36.031207.124139
Johnson, C. M., Ludois, J. M., Beard, B. L., Beukes, N. J., and Heimann, A., 2013 Iron formation carbonates: Paleoceanographic proxy or recorder of microbial diagenesis?: Geology, v. 41, n. 11, p. 1147–1150, https://doi.org/10.1130/G34698.1
Kappler, A., Pasquero, C., Konhauser, K. O., and Newman, D. K., 2005, Deposition of banded iron

formations by anoxygenic phototrophic Fe(II)-oxidizing bacteria: Geology, v. 33, n. 11, p. 865–868, https://doi.org/10.1130/G21658.1
Kappler, A., Johnson, C. M., Crosby, H. A., Beard, B. L., and Newman, D. K., 2010, Evidence for equilibrium iron isotope fractionation by nitrate-reducing iron(II)-oxidizing bacteria: Geochimica et Cosmochimica Acta, v. 74, n. 10, p. 2826–2842, https://doi.org/10.1016/j.gca.2010.02.017
Karhu, J., and Epstein, S., 1986, The Implication of the Oxygen Isotope Records in Coexisting Cherts and Phosphates: Geochimica et Cosmochimica Acta, v. 50, n. 8, p. 1745–1756, https://doi.org/10.1016/0016-7037(86)90136-5
Kendall, B., Reinhard, C. T., Lyons, T. W., Kaufman, A. J., Poulton, S. W., and Anbar, A. D., 2010, Pervasive oxygenation along late Archaean ocean margins: Nature Geoscience, v. 3, p. 647–652, https://doi.org/10.1038/ngeo942
Knauth, L. P., 1979, A Model for the Origin of Chert in Limestone: Geology, v. 7, n. 6, p. 274–277, https://doi.org/10.1130/0091-7613(1979)7<274:AMFTOO>2.0.CO;2
Knauth, L. P., and Lowe, D. R., 2003, High Archean climatic temperature inferred from oxygen isotope geochemistry of cherts in the 3.5 Ga Swaziland Supergroup, South Africa: GSA Bulletin, v. 115, n. 5, p. 566–580, https://doi.org/10.1130/0016-7606(2003)115<0566:HACTIF>2.0.CO;2
Knoll, A. H., and Beukes, N. J., 2009, Introduction: Initial investigations of a Neoarchean shelf margin-basin transition (Transvaal Supergroup, South Africa): Precambrian Research, v. 169, n. 1–4, p. 1–14, https://doi.org/10.1016/j.precamres.2008.10.009
Konhauser, K. O., Hamade, T., Raiswell, R., Morris, R. C., Ferris, F. G., Southam, G., and Canfield, D. E., 2002, Could bacteria have formed the Precambrian banded iron formations?: Geology, v. 30, n. 12, p. 1079–1082, https://doi.org/10.1130/0091-7613(2002)030<1079:CBHFTP>2.0.CO;2
Kurzweil, F., Drost, K., Pasava, J., Wille, M., Taubald, H., Schoeckle, D., and Schoenberg, R., 2015a, Coupled sulfur, iron and molybdenum isotope data from black shales of the Teplá-Barrandian unit argue against deep ocean oxygenation during the Ediacaran: Geochimica et Cosmochimica Acta, v. 171, p. 121–142, https://doi.org/10.1016/j.gca.2015.08.022
Kurzweil, F., Wille, M., Schoenberg, R., Taubald, H., and Van Kranendonk, M. J., 2015b, Continuously increasing δ^{98} Mo values in Neoarchean black shales and iron formations from the Hamersley Basin: Geochimica et Cosmochimica Acta, v. 164, p. 523–542, https://doi.org/10.1016/j.gca.2015.05.009
Kurzweil, F., Wille, M., Gantert, N., Beukes, N. J., and Schoenberg, R., 2016, Manganese oxide shuttling in pre-GOE oceans - evidence from molybdenum and iron isotopes: Earth and Planetary Science Letters, v. 452, p. 69–78, https://doi.org/10.1016/j.epsl.2016.07.013
Landing, W. M., and Bruland, K. W., 1987, The Contrasting Biogeochemistry of Iron and Manganese in the Pacific-Ocean: Geochimica et Cosmochimica Acta, v. 51, n. 1, p. 29–43, https://doi.org/10.1016/0016-7037(87)90004-4
Li, W. Q., Beard, B. L., and Johnson, C. M., 2015, Biologically recycled continental iron is a major component in banded iron formations: Proceedings of the National Academy of Sciences of the United States of America, v. 112, n. 27, p. 8193–8198, https://doi.org/10.1073/pnas.1505515112
Luo, G., Ono, S., Beukes, N. J., Wang, D. T., Xie, S., and Summons, R. E., 2016, Rapid oxygenation of Earth's atmosphere 2.33 billion years ago: Science Advances, v. 2, n. 5, https://doi.org/10.1126/sciadv.1600134
Lyons, T. W., and Severmann, S., 2006, A critical look at iron paleoredox proxies: New insights from modern euxinic marine basins: Geochimica et Cosmochimica Acta, v. 70, n. 23, p. 5698–5722, https://doi.org/10.1016/j.gca.2006.08.021
Maliva, R. G., and Siever, R., 1988, Pre-Cenozoic Nodular Cherts: Evidence for Opal-Ct Precursors and Direct Quartz Replacement: American Journal of Science, v. 288, n. 8, p. 798–809, https://doi.org/10.2475/ajs.288.8.798
——— 1989, Nodular Chert Formation in Carbonate Rocks: The Journal of Geology, v. 97, n. 4, p. 421–433, https://doi.org/10.1086/629320
Marcus, M. A., Westphal, A. J., and Fakra, S. C., 2009, Classification of Fe-bearing species from K-edge XANES data using two-parameter correlation plots. Erratum, (v. 15, p. 463, 2008): Journal of Synchrotron Radiation, v. 16, p. 439–439, https://doi.org/10.1107/S0909049509007328
Martin, J. H., Gordon, R. M., and Fitzwater, S. E., 1990, Iron in Antarctic Waters: Nature. v. 345, p. 156–158, https://doi.org/10.1038/345156a0
Matthews, A., Morgans-Bell, H. S., Emmanuel, S., Jenkyns, H. C., Erel, Y., and Halicz, L., 2004, Controls on iron-isotope fractionation in organic-rich sediments (Kimmeridge Clay, Upper Jurassic, southern England): Geochimica et Cosmochimica Acta, v. 68, n. 14, p. 3107–3123, https://doi.org/10.1016/j.gca.2004.01.019
McManus, J., Berelson, W. M., Severmann, S., Poulson, R. L., Hammond, D. E., Klinkhammer, G. P., and Holm, C., 2006, Molybdenum and uranium geochemistry in continental margin sediments: Paleoproxy potential: Geochimica et Cosmochimica Acta, v. 70, n. 18, p. 4643–4662, https://doi.org/10.1016/j.gca.2006.06.1564
Mettler, S., ms, 2002, *In situ* removal of iron from groundwater: Fe(II) oxygenation, and precipitation products in a calcareous aquifer: Zurich, Switzerland, Swiss Federal Insitute of Technology Zurich, p. 158, https://doi.org/10.3929/ethz-a-004453456
Mettler, S., Wolthers, M., Charlet, L., and von Gunten, U., 2009, Sorption and catalytic oxidation of Fe(II) at the surface of calcite: Geochimica et Cosmochimica Acta, v. 73, n. 7, p. 1826–1840, https://doi.org/10.1016/j.gca.2009.01.003
Miyano, T., and Beukes, N. J., 1984, Phase relations of stilpnomelane, ferriannite, and riebeckite in very low-grade metamorphosed iron-formations: Transactions of the Geological Society of South Africa, v. 87, p. 111–124.
Morris, R. C., 1993, Genetic Modeling for Banded Iron-Formation of the Hamersley Group, Pilbara Craton,

Western-Australia: Precambrian Research, v. 60, n. 1–4, 243–286, https://doi.org/10.1016/0301-9268(93)90051-3
Munoz, M., De Andrade, V., Vidal, O., Lewin, E., Pascarelli, S., and Susini, J., 2006, Redox and speciation micromapping using dispersive X-ray absorption spectroscopy: Application to iron chlorite mineral of a metamorphic rock thin section: Geochemistry, Geophysics, Geosystems, v. 7, n. 11, https://doi.org/10.1029/2006GC001381
O'Day, P. A., Rivera, N., Jr., Root, R., and Carroll, S. A., 2004, X-ray absorption spectroscopic study of Fe reference compounds for the analysis of natural sediments: American Mineralogist, v. 89, n. 4, p. 572–585, https://doi.org/10.2138/am-2004-0412
Pascarelli, S., Neisius, T., and De Panfilis, S., 1999, Turbo-XAS: Dispersive XAS using sequential acquisition: Journal of Synchrotron Radiation, v. 6, 1044–1050, https://doi.org/10.1107/S0909049599004513
Pascarelli, S., Mathon, O., Mairs, T., Kantor, I., Agostini, G., Strohm, C., Pasternak, S., Perrin, F., Berruyer, G., Chappelet, P., Clavel, C., and Dominguez, M. C., 2016, The Time-resolved and Extreme-conditions XAS (TEXAS) facility at the European Synchrotron Radiation Facility: The energy-dispersive X-ray absorption spectroscopy beamline ID24: Journal of Synchrotron Radiation, v. 23, p. 353–368, https://doi.org/10.1107/S160057751501783X
Pearce, J. A., 1983, Role of the sub-continental lithosphere in magma genesis at active continental margins, *in* Hawkesworth, C. J., and Norry, M. J., editors, Continental Basalts and Mantle Xenoliths: Nantwich, United Kingdom, Shiva Press, p. 230–249.
Planavsky, N., Rouxel, O. J., Bekker, A., Hofmann, A., Little, C. T. S., and Lyons, T. W., 2012, Iron isotope composition of some Archean and Proterozoic iron formations: Geochimica et Cosmochimica Acta, v. 80, p. 158–169, https://doi.org/10.1016/j.gca.2011.12.001
Polyakov, V. B., and Mineev, S. D., 2000, The use of Mossbauer spectroscopy in stable isotope geochemistry: Geochimica et Cosmochimica Acta, v. 64, n. 5, p. 849–865, https://doi.org/10.1016/S0016-7037(99)00329-4
Poulson, R. L., Siebert, C., McManus, J., and Berelson, W. M., 2006, Authigenic molybdenum isotope signatures in marine sediments: Geology, v. 34, n. 8, p. 617–620, https://doi.org/10.1130/G22485.1
Préat, A. R., De Jong, J. T. M., De Ridder, C., and Gillan, D. C., 2011, Possible Fe Isotope Fractionation During Microbiological Processing in Ancient and Modern Marine Environments, *in* Tewari, V., and Seckbach, J., editors, STROMATOLITES: Interaction of Microbes with Sediments: Dordrecht, Netherlands, Springer Netherlands, Cellular Origin, Life in Extreme Habitats and Astrobiology, v. 18, p. 651–673, https://doi.org/10.1007/978-94-007-0397-1_29
Raiswell, R., and Canfield, D. E., 1998, Sources of iron for pyrite formation in marine sediments: American Journal of Science, v. 298, n. 3, p. 219–245, https://doi.org/10.2475/ajs.298.3.219
Ravel, B., and Newville, M., 2005, ATHENA, ARTEMIS, HEPHAESTUS: Data analysis for X-ray absorption spectroscopy using *IFEFFIT*: Journal of Synchrotron Radiation, v. 12, p. 537–541, https://doi.org/10.1107/S0909049505012719
Reeder, R. J., 1983, Crystal chemistry of the rhombohedral carbonates, *in* Reeder, R., editor, Carbonates: Mineralogy and Chemistry: Reviews in Mineralogy and Geochemistry, v. 11, n. 1, p. 1–47.
Riding, R., Fralick, P., and Liang, L. Y., 2014, Identification of an Archean marine oxygen oasis: Precambrian Research, v. 251, p. 232–237, https://doi.org/10.1016/j.precamres.2014.06.017
Rouxel, O. J., Bekker, A., and Edwards, K. J., 2005, Iron isotope constraints on the Archean and Paleoproterozoic ocean redox state: Science, v. 307, n. 5712, p. 1088–1091, https://doi.org/10.1126/science.1105692
——— 2006, Response to comment on "Iron isotope constraints on the Archean and Paleoproterozoic ocean redox state": Science, v. 311, n. 5758, https://doi.org/10.1126/science.1118420
Rouxel, O., Sholkovitz, E., Charette, M., and Edwards, K. J., 2008, Iron isotope fractionation in subterranean estuaries: Geochimica et Cosmochimica Acta, v. 72, n. 14, p. 3413–3430, https://doi.org/10.1016/j.gca.2008.05.001
Rudnick, R. L., and Gao, S., 2004, Composition of the Continental Crust, *in* Rudnick, R. L., The Crust: Treatise on Geochemistry, v. 3, p. 1–64, https://doi.org/10.1016/B0-08-043751-6/03016-4
Schauble, E. A., 2004, Applying Stable Isotope Fractionation Theory to New Systems, *in* Johnson, C. M., Beard, B. L., and Albarede, F., editors, Geochemistry of Non-Traditional Stable Isotopes: Reviews in Mineralogy and Geochemistry, v. 55, p. 65–111, https://doi.org/10.2138/gsrmg.55.1.65
Schoenberg, R., and von Blanckenburg, F., 2005, An assessment of the accuracy of stable Fe isotope ratio measurements on samples with organic and inorganic matrices by high-resolution multicollector ICP-MS: International Journal of Mass Spectrometry, v. 242, n. 2–3, p. 257–272, https://doi.org/10.1016/j.ijms.2004.11.025
——— 2006, Modes of planetary-scale Fe isotope fractionation: Earth and Planetary Science Letters, v. 252, n. 3–4, p. 342–359, https://doi.org/10.1016/j.epsl.2006.09.045
Schröder, S., Lacassie, J. P., and Beukes, N. J., 2006, Stratigraphic and geochemical framework of the Agouron drill cores, Transvaal Supergroup (Neoarchean-Paleoproterozoic, South Africa): South African Journal of Geology, v. 109, n. 1–2, p. 23–54, https://doi.org/10.2113/gssajg.109.1-2.23
Schwertmann, U., and Cornell, R. M., 2000, Iron Oxides in the Laboratory: Preparation and Characterization: Weinheim, Germany, Wiley-VCH Verlag GmbH, 188 p., https://doi.org/10.1002/9783527613229
Severmann, S., Johnson, C. M., Beard, B. L., and McManus, J., 2006, The effect of early diagenesis on the Fe isotope compositions of porewaters and authigenic minerals in continental margin sediments: Geochimica et Cosmochimica Acta, v. 70, n. 8, p. 2006–2022, https://doi.org/10.1016/j.gca.2006.01.007
Severmann, S., Lyons, T. W., Anbar, A., McManus, J., and Gordon, G., 2008, Modern iron isotope perspective on the benthic iron shuttle and the redox evolution of ancient oceans: Geology, v. 36, n. 6, p. 487–490, https://doi.org/10.1130/G24670A.1
Severmann, S., McManus, J., Berelson, W. M., and Hammond, D. E., 2010, The continental shelf benthic

iron flux and its isotope composition: Geochimica et Cosmochimica Acta, v. 74, n. 14, p. 3984–4004, https://doi.org/10.1016/j.gca.2010.04.022
Siebert, C., McManus, J., Bice, A., Poulson, R., and Berelson, W. M., 2006, Molybdenum isotope signatures in continental margin marine sediments: Earth and Planetary Science Letters, v. 241, n. 3–4, p. 723–733, https://doi.org/10.1016/j.epsl.2005.11.010
Solé, V. A., Papillon, E., Cotte, M., Walter, P., and Susini, J., 2007, A multiplatform code for the analysis of energy-dispersive X-ray fluorescence spectra: Spectrochimica Acta Part B: Atomic Spectroscopy, v. 62, n. 1, p. 63–68, https://doi.org/10.1016/j.sab.2006.12.002
Staubwasser, M., von Blanckenburg, F., and Schoenberg, R., 2006, Iron isotopes in the early marine diagenetic iron cycle: Geology, v. 34, n. 8, p. 629–632, https://doi.org/10.1130/G22647.1
Steinhoefel, G., von Blanckenburg, F., Horn, I., Konhauser, K. O., Beukes, N. J., and Gutzmer, J., 2010, Deciphering formation processes of banded iron formations from the Transvaal and the Hamersley successions by combined Si and Fe isotope analysis using UV femtosecond laser ablation: Geochimica et Cosmochimica Acta, v. 74, n. 9, p. 2677–2696, https://doi.org/10.1016/j.gca.2010.01.028
Sumner, D., 2002, Neoarchean Carbonates - Clues to Early Life and Early Ocean Chemistry: Johannesburg, South Africa, Rand Afrikaans University, International Associate of Sedimentologists, 16th International Sedimentological Congress, 25 p.
Sumner, D. Y., and Beukes, N. J., 2006, Sequence stratigraphic development of the Neoarchean Transvaal carbonate platform, Kaapvaal Craton, South Africa: South African Journal of Geology, v. 109, n. 1–2, p. 11–22, https://doi.org/10.2113/gssajg.109.1-2.11
Sumner, D. Y., and Grotzinger, J. P., 1996, Were kinetics of Archean calcium carbonate precipitation related to oxygen concentration?: Geology, v. 24, n. 2, p. 119–122, https://doi.org/10.1130/0091-7613(1996)024<0119:WKOACC>2.3.CO;2
——— 2004, Implications for Neoarchaean ocean chemistry from primary carbonate mineralogy of the Campbellrand-Malmani Platform, South Africa: Sedimentology, v. 51, n. 6, p. 1273–1299, https://doi.org/10.1111/j.1365-3091.2004.00670.x
Swanner, E. D., Mloszewska, A. M., Cirpka, O. A., Schoenberg, R., Konhauser, K. O., and Kappler, A., 2015a, Modulation of oxygen production in Archaean oceans by episodes of Fe(II) toxicity: Nature Geoscience, v. 8, p. 126–130, https://doi.org/10.1038/ngeo2327
Swanner, E. D., Wu, W. F., Schoenberg, R., Byrne, J., Michel, F. M., Pan, Y. X., and Kappler, A., 2015b, Fractionation of Fe isotopes during Fe(II) oxidation by a marine photoferrotroph is controlled by the formation of organic Fe-complexes and colloidal Fe fractions: Geochimica et Cosmochimica Acta, v. 165, p. 44–61, https://doi.org/10.1016/j.gca.2015.05.024
Taylor, P. D. P., Maeck, R., and De Bièvre, P., 1992, Determination of the Absolute Isotopic Composition and Atomic-Weight of a Reference Sample of Natural Iron: International Journal of Mass Spectrometry and Ion Processes, v. 121, n. 1–2, p. 111–125, https://doi.org/10.1016/0168-1176(92)80075-C
Taylor, S. R., and MacLennan, S. H., 1985, The Continental Crust: Its Composition and Evolution: Oxford, Blackwell, 312 p.
Tosca, N. J., Guggenheim, S., and Pufahl, P. K., 2016, An authigenic origin for Precambrian greenalite: Implications for iron formation and the chemistry of ancient seawater: GSA Bulletin, v. 128, n. 3–4, p. 511–530, https://doi.org/10.1130/B31339.1
Truswell, J. F., and Eriksson, K. A., 1975, A palaeoenvironmental interpretation of the Early Proterozoic Malmani Dolomite from Zwartkops, South Africa: Precambrian Research, v. 2, n. 3, p. 277–303, https://doi.org/10.1016/0301-9268(75)90013-3
van den Boorn, S. H. J. M., ms, 2008, Silicon isotopes and the origin of Archaean cherts: The Netherlands, University of Utrecht, Ph. D. thesis, p. 277.
van der Zee, C., Roberts, D. R., Rancourt, D. G., and Slomp, C. P., 2003, Nanogoethite is the dominant reactive oxyhydroxide phase in lake and marine sediments: Geology, v. 31, n. 11, p. 993–996, https://doi.org/10.1130/G19924.1
Veizer, J., 1983, Chemical diagenesis of carbonates: Theory and application of trace element techniques, *in* Arthur, M. A., Anderson, T. F., Kaplan, I. R., Veizer, J., and Land, L.S., editors, Stable Isotopes in Sedimentary Geology: Society of Economic Paleontologists and Mineralogists Short Course Notes, p. III-1-III-100.
Voegelin, A. R., Nagler, T. F., Beukes, N. J., and Lacassie, J. P., 2010, Molybdenum isotopes in late Archean carbonate rocks: Implications for early Earth oxygenation: Precambrian Research, v. 182, n. 1–2, p. 70–82, https://doi.org/10.1016/j.precamres.2010.07.001
von Blanckenburg, F., Marnberti, M., Schoenberg, R., Kamber, B. S., and and Webb, G. E., 2008, The iron isotope composition of microbial carbonate: Chemical Geology, v. 249, n. 1–2, p. 113–128, https://doi.org/10.1016/j.chemgeo.2007.12.001
Wang, K., Savage, P. S., and Moynier, F., 2014, The iron isotope composition of enstatite meteorites: Implications for their origin and the metal/sulfide Fe isotopic fractionation factor: Geochimica et Cosmochimica Acta, v. 142, p. 149–165, https://doi.org/10.1016/j.gca.2014.07.019
Webb, G. E., and Kamber, B. S., 2000, Rare earth elements in Holocene reefal microbialites: A new shallow seawater proxy: Geochimica et Cosmochimica Acta, v. 64, n. 9, p. 1557–1565, https://doi.org/10.1016/S0016-7037(99)00400-7
Weyer, S., Anbar, A. D., Brey, G. P., Münker, C., Mezger, K., and Woodland, A. B., 2005, Iron isotope fractionation during planetary differentiation: Earth and Planetary Science Letters, v. 240, n. 2, p. 251–264, https://doi.org/10.1016/j.epsl.2005.09.023
Wilkin, R. T., and Barnes, H. L., 1997, Formation processes of framboidal pyrite: Geochimica et Cosmochimica, Acta, v. 61, n. 2, p. 323–339, https://doi.org/10.1016/S0016-7037(96)00320-1
Wille, M., Kramers, J. D., Nagler, T. F., Beukes, N. J., Schröder, S., Meisel, Th., Lacassie, J. P., and Voegelin, A. R., 2007, Evidence for a gradual rise of oxygen between 2.6 and 2.5 Ga from Mo isotopes and Re-PGE

signatures in shales: Geochimica et Cosmochimica Acta, v. 71, n. 10, p. 2417–2435, https://doi.org/10.1016/j.gca.2007.02.019

Yamaguchi, K. E., and Ohmoto, H., 2006, Comment on "Iron isotope constraints on the Archean and Paleoproterozoic ocean redox state": Science, v. 311, n. 5758, p. 177, https://doi.org/10.1126/science.1118221

Yamaguchi, K. E., Johnson, C. M., Beard, B. L., and Ohmoto, H., 2005, Biogeochemical cycling of iron in the Archean-Paleoproterozoic Earth: Constraints from iron isotope variations in sedimentary rocks from the Kaapvaal and Pilbara Cratons: Chemical Geology, v. 218, p. 135–169, https://doi.org/10.1016/j.chemgeo.2005.01.020